Probability-Perturbation McMC for 3D Bayesian TDEM Inversion with Unknown Covariance Parameters

Liu[1], Z., Yin[1], Z., Kloeckner[1], J., Muir[2], J., and Caers[1], J.,

[1]Mineral-X, Department of Earth & Planetary Sciences, Stanford University, USA

[2] Fleet Space Technologies, Beverley, South Australia, Australia

Corresponding Author: Jef Caers, jcaers@stanford.edu, 450 Jane Stanford Way, Stanford, CA 94305, USA

Preprint notice: This manuscript is a preprint and **has not** undergone peer review. Its content may be revised in response to further analysis and peer-review comments. A subsequent version may differ from the present manuscript. This preprint record will be updated with the DOI of the peer-reviewed article upon publication.

Abstract

We present a hierarchical Bayesian inversion framework for large-scale 3D time-domain electromagnetic (TDEM) data that jointly infers the subsurface conductivity field and the parameters controlling a Gaussian process (GP) covariance function, requiring minimal assumptions about subsurface spatial structure. The framework addresses two fundamental bottlenecks in 3D probabilistic inversion: the curse of dimensionality in high-dimensional model space, resolved through GP parameterization that encodes spatial continuity in a compact set of hyperparameters; and the prohibitive cost of repeated forward evaluations, resolved through a 3D surrogate that replaces the PDE-based solver during McMC sampling. Posterior sampling is performed via the Probability Perturbation Method (PPM) within a Metropolis-Hastings algorithm augmented with delayed rejection and adaptive annealing, which together balance global exploration and local posterior refinement. Prior falsification through Principal Components Analysis (PCA) ensures the training ensemble covers the data-consistent region of model space before inversion begins. We validate the framework on synthetic experiments of increasing complexity and demonstrate its application to field TDEM data from a greenfield Ni-Cu-Co sulfide exploration target in the Midcontinent Rift system. The surrogate reduces the per-iteration forward cost by a factor of approximately 10^4 relative to the full PDE solver, making 50,000-iteration 3D McMC chains tractable on a single workstation. The resulting posterior ensemble enables full 3D uncertainty quantification, interpretable GP-parameter recovery, and loss-based false-positive screening of subsurface anomalies.

Keywords: Time-Domain Electromagnetic, Bayesian Inversion, Gaussian Process, Uncertainty Quantification, Surrogate Modeling, Probability Perturbation Method, Critical Mineral Exploration

1. Introduction

Three-dimensional (3D) time-domain electromagnetic (TDEM) methods are critical tools in critical mineral exploration, groundwater assessment, and structural geological mapping (e.g., Yang and Oldenburg, 2012; Auken et al., 2015; Christensen et al., 2017; Knight et al., 2018; Kwan and Reford, 2025;), owing to their high sensitivity to subsurface electrical conductivity variations (Nabighian, 1979). Traditionally, the interpretation of 3D TDEM data relies on deterministic inversion frameworks, which seek a single, optimal conductivity model by minimizing a data misfit function subject to regularized mathematical constraints and subjective assumptions (Tikhonov, 1963). While computationally viable, deterministic approaches inherently fail to provide a rigorous assessment of non-uniqueness and uncertainty, which are pervasive in geophysical inverse problems due to noisy observations and limited spatial data coverage (Tarantola and Valette, 1982; Mosegaard and Tarantola, 1995; Tarantola, 2005).

To quantify these uncertainties, probabilistic inversion frameworks, particularly Bayesian inference solved via Markov chain Monte Carlo (McMC, Gelfand and Smith, 1990) methods, have been extensively utilized. By treating subsurface properties as random variables, Bayesian methods provide a comprehensive posterior distribution that maps out a group of plausible models from geophysical data's perspective (Sambridge and Mosegaard, 2002). However, the practical application of 3D Bayesian inversion to large-scale TDEM datasets remains severely hindered by a double computational and mathematical bottlenecks. First, the curse of dimensionality poses a massive sampling challenge. To resolve complex 3D geological structures, the inversion domain is typically discretized into millions of independent voxel cells (Oldenburg and Li, 2005; Haber et al., 2000). Performing unconstrained random walk sampling in such a high-dimensional space is not only computationally intractable but also geophysically problematic, as independent pixel-based perturbations ignore spatial correlations and inevitably result in unstructured, noise-like fields rather than coherent geological bodies (Linde et al., 2015; Laloy et al., 2018). Second, even if plausible models can be sampled, evaluating their data misfit remains prohibitively expensive. Calculating a single 3D forward response requires solving complex, large-scale partial differential equations (PDEs) describing transient electromagnetic wave propagation and diffusion (Börner et al., 2015; Engebretsen et al., 2022), a process that can take up to several hours for a single simulation on refined 3D grids. Because standard McMC algorithms require hundreds of thousands of sequential forward evaluations to ensure chain convergence, a full 3D uncertainty quantification (UQ) workflow can easily demand weeks or even months of computational time.

Consequently, practices in production environments are frequently forced into a compromise: either reverting to deterministic 3D methods that completely lack UQ or substitute full 3D Bayesian inversions with 1D or 2D approximations. While 1D or 2D simplified methods reduce computational runtime, they fundamentally fail to capture the complex, directional 3D spatial relationships and correlations inherent to real geological structures, leading to severe structural misinterpretations. Conversely, even when full 3D stochastic inversions are attempted, standard pixel-based sampling often lacks a structured parameterization framework to govern spatial continuity across millions of grid cells, inevitably yielding geophysically implausible, noise-like models (Walker and Curtis, 2014). Therefore, a truly robust 3D uncertainty quantification framework must satisfy a dual requirement: it must not only bypass the heavy PDE forward modeling cost but also incorporate an efficient 3D spatial parameterization that honors the underlying geological continuity and spatial relationships without inflating the parameter dimensionality.

To address these computational and architectural demands, researchers have increasingly turned to deep generative algorithms. Generative neural networks are favored given their capacity to efficiently sample complex spatial features, rendering them an attractive alternative for approximating rigorous Bayesian solutions (Chan and Elsheikh, 2017; Mo et al., 2020; Mosser et al., 2020). For instance, Variational Autoencoders (VAEs) offer a natural architecture for this purpose, as their encoder-decoder structure can be adapted to map observed EM data directly to a distribution over model parameters. Rodriguez et al. (2023) applied this to 1D MT inversion using a multimodal VAE with a mixture of truncated Gaussian densities, recovering multiple plausible resistivity solutions along with their associated probabilities, thereby explicitly accounting for the non-uniqueness inherent in EM inversion. Pushing towards 3D, Liu et al. (2025) adopted the variational inference framework underpinning VAEs, while replacing the learned encoder and decoder with a physics-based inversion optimizer and forward solver respectively, to approximate the posterior of a 3D MT problem as a Gaussian distribution. While VAEs effectively encode complex geological patterns into a compact latent space, recovering the posterior for each new dataset still requires solving a per-observation optimization problem within that latent space (Laloy et al., 2018; Lopez-Alvis et al., 2022). Unlike VAEs, Invertible Neural Networks (INNs) construct strictly bijective mappings between model and data spaces, training the forward process and extracting the inverse implicitly through invertibility, such that posterior samples are obtained via inexpensive backward passes rather than per-dataset optimization (Ardizzone et al., 2018). Wu et al. (2023) demonstrated this for airborne time-domain EM, introducing an explicit noise variable alongside the latent variable to account for data uncertainty, while Bittar et al. (2025) extended the framework to EM well logging for real-time geosteering, introducing a boundary loss term to improve interface delineation. However, these approaches are inherently approximating where the posterior is baked into the network weights implicitly during training rather than derived from first principles for each observation. For applications demanding rigorous uncertainty quantification, this approximations have difficulties to be formally bounded or justified.

To preserve the mathematical rigor of Bayesian inference while achieving computational tractability, an alternative strategy replaces only the expensive PDE solver with a learned deep neural network surrogate (Wu et al., 2023), while retaining McMC as the inference engine (e.g., Moghadas et al., 2020; Yang et al., 2024; Liu et al., 2026). Unlike direct generative inversion, this hybrid framework maintains an explicit likelihood evaluation at every McMC step, ensuring that accepted posterior samples are formally conditioned on the actual observation. Nevertheless, this approach immediately confronts a fundamental tension in model parameterization. Training a forward surrogate requires a representative ensemble of physically plausible subsurface models for both training and posterior sampling. As aforementioned, unconstrained pixel-based perturbations produce geologically unrealistic fields rather than coherent geological bodies. To sidestep this problem, traditional surrogate-accelerated inversions impose oversimplified structural parameterizations, including homogeneous blocks, sharp horizontal layers, or fixed geometric primitives (e.g., McMillan et al., 2015; Puzyrev and Swidinsky, 2021), which enforce spatial coherence but at the cost of geological realism. The central parameterization challenge that this work addresses is therefore how to preserve full 3D voxel fidelity as the surrogate input while simultaneously constraining the MCMC sampling space to geologically realistic fields.

Resolving this parameterization challenge requires a careful re-evaluation of prior models in Bayesian geophysical inversion (Tarantola, 2005; Linde et al., 2015). From the perspective of Bayesian inversion theory, the subsurface conductivity distribution is naturally regarded as a function-valued unknown, where the objective is to infer a posterior distribution over spatial fields rather than individual discretized parameters (Stuart, 2010; Bui-Thanh et al., 2013). Therefore, practical inversion required prior representations that define probability measures over spatial functions while remaining computationally tractable after discretization. While discrete prior models such as multiple-point statistics (MPS, Strebelle, 2002; Mariethoz and Caers, 2015) or level-set methods (Aghasi et al., 2011; Zheglova et al., 2013; Giraud et al., 2021) can capture intricate geological boundaries, they are notoriously difficult to parameterize continuously for neural network training. Spatial fields governed by a Gaussian process (GP) offer a more tractable function-space alternative (Kitanidis, 1996; Wang et al., 2022). By encoding spatial continuity through a covariance function, a GP defines a probability distribution over the entire 3D conductivity field through a compact set of hyperparameters, naturally constraining the surrogate input dimensionality while preserving geologically realistic heterogeneity (Kitanidis, 1996). However, a conventional GP inversion still relies on a fixed, pre-defined covariance function (Kitanidis, 1995; Hansen et al., 2014). In under-explored frontiers where spatial correlation lengths, variances, and directional orientations are unknown a priori, fixing these parameters amounts to an unverifiable assumption that can systematically bias the posterior (Kitanidis, 1996; Xiao et al., 2021). Hierarchical Bayesian formulations address this by treating the covariance hyperparameters as additional unknowns to be jointly inferred alongside the conductivity field itself (e.g., Kitanidis, 1986; Xiao et al., 2021; Wang et al., 2022; Polette et al., 2025). Yet simultaneously sampling both the structural hyperparameters and the high-dimensional spatial field within a computationally feasible 3D McMC framework, particularly when forward evaluations must themselves be accelerated by a surrogate, remains an outstanding challenge and, to our knowledge, has not been demonstrated for large-scale 3D EM inversion.

In this work, we propose a hierarchical Bayesian inversion framework for large-scale 3D TDEM data that jointly infers the subsurface conductivity field and the parameters controlling the GP covariance function (GP-parameters hereafter), requiring only minimal assumptions about the subsurface spatial structure. A falsification based on Principal Component Analysis (PCA) is first performed to constrain the plausible prior GP-parameter space. Then, prior GP-parameter samples drawn from this constrained space are used to generate prior 3D conductivity realizations, on which numerical EM forward simulations are run to produce training pairs for the surrogate that replaces expensive PDE solves during subsequent McMC sampling. Posterior sampling is performed via a data-conditioned perturbation scheme that generates geologically coherent proposals within a Metropolis-Hastings algorithm, further combined with delayed rejection to improve mixing efficiency in the high-dimensional model space. The resulting posterior ensemble enables full 3D uncertainty quantification and false-positive screening of subsurface anomalies. We validate the framework on both synthetic experiments and field TDEM data sets, demonstrating that rigorous 3D probabilistic inversion is achievable in exploration settings where little to no prior geological knowledge is available.

2. Geological Setting and Field Data Description

The field data used in this study was acquired from an actual greenfield exploration targeting Nickel-Sulfide deposits in the Midcontinent Rift system, a Mesoproterozoic tectonic feature extending approximately 2,000 km across the north-central United States and Canada, formed by large-scale continental rifting approximately 1.1 billion years ago (Cannon, 1992). The rift system hosts several known magmatic Ni-Cu-Co-PGE sulfide deposits associated with large mafic-ultramafic intrusions, where dense and highly conductive massive sulfide mineralization is expected to concentrate at the base of intrusions due to gravitational settling during magmatic differentiation (Barnes et al., 2016; Lightfoot and Evans-Lamswood, 2015). The exploration target in this study is a set of prospective conductor anomalies within such an intrusive setting. No drill holes intersecting the presented targets are available for this work, making this a true greenfield scenario with no direct subsurface constraint on the geometry or depth of the conductors.

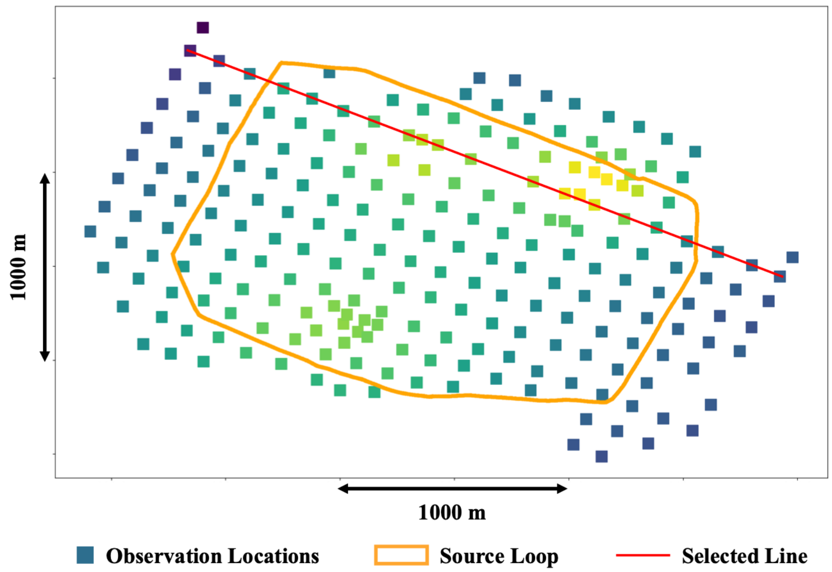

Figure 1. Illustration map of survey geometry and location of selected profile.

A ground loop TDEM survey was acquired in the study area, and the survey geometry is shown in Figure 1. The transmitter is a roughly 2,000 m × 1,500 m rectangular ground loop positioned to maximize coupling with the target conductor anomalies. The survey collected multi-channel transient EM data at stations distributed across the survey area, measuring the decay of the induced magnetic field response in the vertical direction. The full dataset comprises 43 time channels spanning a wide range of delay times after transmitter current shutoff. For the inversion presented in this study, 12 time channels are selected, corresponding to channels 28th through 39th of the original dataset. The earliest channels (1–27) are excluded because they are dominated by very shallow subsurface responses and are susceptible to noise associated with human activities (Nabighian and James, 1991; Auken et al., 2015). The latest channels (40–43) are excluded because they correspond to delay times at which the transient signal has decayed to levels potentially dominated by noise and carries information primarily about depths beyond the target of interest (Spies, 1989). The selected 12 channels therefore represent the optimal window for resolving the target conductors at intermediate depths while maintaining an acceptable signal-to-noise ratio. Data errors were estimated from repeated measurements and assigned as channel- and station-specific standard deviations, used subsequently in the inversion likelihood evaluation.

For the 3D inversion presented in this study, a single survey profile is selected as a proof-of-concept demonstration of the framework, whereas the extension to full multi-line 3D inversion is discussed in Section 6. This line was chosen because it is sufficiently long to provide spatial resolution of the conductor geometry and directly intersects two primary EM anomalies of interest (Yin et al., 2025), with 19 receiver stations located along the profile. The observed TDEM data along this profile across all 12 selected time channels are shown in Figure 2.

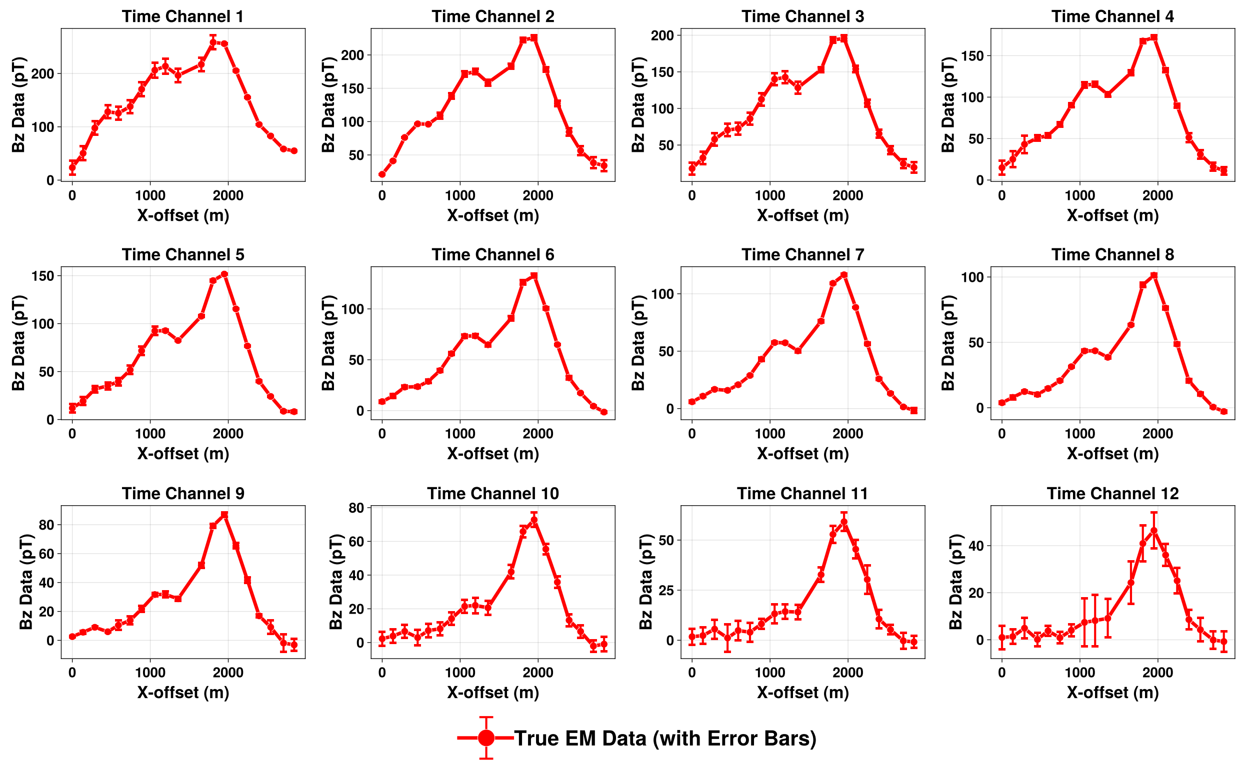

Figure 2. The ground TDEM data used in this work, with selected time channels.

From this data profile, two prominent anomalies are visible. The first one is characterized by a strong amplitude peak at intermediate offset rightward from the profile center. The coherence of this anomaly across all 12 selected channels indicates a conductor with substantial conductance, persisting well into the late-time diffusive regime. The other one is located to the left side and decays in amplitude with increasing time, indicating a smaller and shallower conductor. The signal-to-noise ratio (SNR) is high in the early-to-mid selected channels and decreases progressively at later times, consistent with the diminishing transient amplitude at longer delay times.

The conductor anomaly targeted in this study is one of several identified in the broader survey area. Previous work on this dataset by Yin et al. (2025) inverted the multi-conductor field data using parametric geometric models, which demonstrated significant uncertainty reduction in conductor depth and volume estimates relative to simple prior assumptions. The present study adopts a fundamentally different parameterization: rather than assuming a specific geometric shape, we treat the 3D subsurface conductivity as a continuous spatial field governed by a Gaussian process with unknown covariance structure, enabling full voxel-resolution inversion and uncertainty quantification without geometric simplification.

3. Methodology

For a TDEM survey, the primary objective is to characterize the subsurface geoelectrical structure. Let $\boldsymbol{m} \in \mathbb{R}^{\boldsymbol{M}}$ denote the 3D subsurface conductivity model in log-scale that discretized on a regular voxel grid of $\boldsymbol{M}$ cells and let $\boldsymbol{d^{obs}} \in \mathbb{R}^{\boldsymbol{N}}$ denote the observed TDEM data. The forward problem is defined by the non-linear operator $\boldsymbol{\mathcal{F}}(\cdot)$ such that

$$\boldsymbol{d} = \boldsymbol{\mathcal{F}}(\boldsymbol{m}) + \boldsymbol{\varepsilon}, \tag{1}$$

where evaluating $\boldsymbol{\mathcal{F}}(\cdot)$ requires solving the governing PDEs for transient EM wave propagation, and $\boldsymbol{\varepsilon}$ represents data errors that commonly assumed to follow a Gaussian distribution. Rather than seeking a single optimal $\boldsymbol{m}$, we adopt a Bayesian formulation and characterize the posterior distribution,

$$\boldsymbol{p}(\boldsymbol{m}|\boldsymbol{d^{obs}}) \propto \boldsymbol{p}(\boldsymbol{d^{obs}}|\boldsymbol{m})\boldsymbol{p}(\boldsymbol{m}), \tag{2}$$

where $\boldsymbol{p}(\boldsymbol{d^{obs}}|\boldsymbol{m})$ is the likelihood function encoding data misfit, and $\boldsymbol{p}(\boldsymbol{m})$ is the prior distribution. We parameterize the prior as a Gaussian process and will explain the detail of parameterization in the following section. Since $\boldsymbol{\theta}$ is unknown in greenfield settings, we treat it as an additional unknown and target the joint posterior as

$$p(\boldsymbol{m}, \boldsymbol{\theta}|\boldsymbol{d}^{obs}). \tag{3}$$

Thus, the problem is set as the search for this joint posterior. The following subsections describe the six components of our framework for sampling this joint posterior efficiently.

3.1. Parameterization of 3D Voxel Conductivity Model

From the perspective of Bayesian inverse theory, the subsurface log-conductivity distribution can be regarded as a function-valued unknown, with the voxel model m representing its finite-dimensional discretization on the inversion grid (Stuart, 2010; Bui-Thanh et al., 2013). To maintain geological coherence and avoid the curse of dimensionality in high-dimensional McMC sampling, we parameterize $\boldsymbol{m}$ as a realization of a GP, which defines a probability distribution over spatial conductivity fields through its covariance function, thereby encoding spatial continuity while describing the field statistics using a compact set of GP-parameters $\boldsymbol{\theta}$ (Kitanidis, 1996; Wang et al., 2022).

Specifically, the 3D log-conductivity field is modeled as a stationary Gaussian random field with a spherical variogram characterized by eight GP-parameters:

$$\boldsymbol{\theta} = \{\boldsymbol{\ell}_{maj}, \boldsymbol{R}_{mid/maj}, \boldsymbol{R}_{min/mid}, \boldsymbol{\phi}_{yaw}, \boldsymbol{\phi}_{pitch}, \boldsymbol{\phi}_{roll}, \boldsymbol{\mu}_{\sigma}, \boldsymbol{s}_{\sigma}\}, \tag{4}$$

where ℓ_{maj} is the major-axis correlation length in meters, $R_{mid/maj} = \ell_{mid}/\ell_{maj}$ and $R_{min/mid} = \ell_{min}/\ell_{mid}$ are the aspect ratios defining the intermediate and minor correlation lengths relative to the major axis; ϕ_{yaw}, ϕ_{pitch}, and ϕ_{roll} are the three bounded ZYX Euler rotation angles that jointly define the three-dimensional orientation of the anisotropic covariance structure. The μ_σ and s_σ are the mean and standard deviation of the conductivity field in natural-log scale. Together, these parameters describe the statistical structure of the 3D conductivity field, including its characteristic spatial scales, anisotropy, orientation, and conductivity distribution. This representation is well suited to prior specification in greenfield settings, where geological information is insufficient to define a more restrictive structural parameterization.

Given $\boldsymbol{\theta}$, a 3D conductivity realization $\boldsymbol{m}$ is generated in two steps:

1. First, a latent random field $\boldsymbol{w} \in \mathbb{R}^M$ is drawn on the full voxel grid $\mathfrak{D}$, where each element of $\boldsymbol{w}$ is an independent standard Gaussian deviate.
2. Second, $\boldsymbol{w}$ is transformed into a spatially correlated Gaussian field through FFT-based sequential Gaussian simulation (FFTSIM, Dietrich and Newsam, 1993), which applies the covariance structure defined by $\boldsymbol{\theta}$ in the Fourier domain.

In this construction, the phase of the Fourier transform of $\boldsymbol{w}$ is combined with the spectral density associated with the variogram to produce a realization with the prescribed spatial correlation, mean, and standard deviation. The latent random field $\boldsymbol{w}$ therefore controls the spatial pattern of a particular realization, whereas $\boldsymbol{\theta}$ controls the statistical structure under which that pattern is expressed. Perturbing $\boldsymbol{w}$ changes the spatial arrangement of conductivity features while keeping the statistical properties defined by $\boldsymbol{\theta}$ fixed, and perturbing $\boldsymbol{\theta}$ changes the covariance structure while the pattern encoded in $\boldsymbol{w}$ is reinterpreted under the new covariance. This separation between spatial pattern ($\boldsymbol{w}$) and statistical structure ($\boldsymbol{\theta}$) is the key property exploited by the PPM-based random walk described in Section 3.4.

The complete set of unknowns targeted by the McMC sampler is therefore $(\boldsymbol{m}, \boldsymbol{\theta})$, or equivalently $(\boldsymbol{w}, \boldsymbol{\theta})$ since $\boldsymbol{m}$ is deterministically generated from $(\boldsymbol{w}, \boldsymbol{\theta})$. The joint posterior $p(\boldsymbol{w}, \boldsymbol{\theta} | \boldsymbol{d}^{obs})$ is sampled by perturbing both $\boldsymbol{w}$ and $\boldsymbol{\theta}$ simultaneously at each McMC iteration, as described in Sections 3.5.

3.2. Falsification of Prior GP-parameters

Before inversion, plausible ranges for the GP-parameters, $\boldsymbol{\theta}$, must be established. In scenarios where only limited amount of direct information about the subsurface is available a priori, any initial specification of the prior ranges for $\boldsymbol{\theta}$ is therefore uncertain and potentially misleading. Critically, if the true posterior

$p(\boldsymbol{m}, \boldsymbol{\theta} | \boldsymbol{d}^{obs})$ lies outside the support of the prior, that is, if no combination of $\boldsymbol{\theta}$ within the specified range can generate forward responses consistent with $\boldsymbol{d}^{obs}$, then no inference method, regardless of its sophistication, can recover the correct posterior from that prior. Falsification is therefore a necessary precondition for valid Bayesian inversion.

Rather than fixing the ranges of GP-parameters arbitrarily and risking the failure mode , we use a two-part procedure consisting of an initial sensitivity screening followed by data-space iterative prior falsification (Tarantola, 2005) to systematically eliminate GP-parameter ranges whose forward responses are inconsistent with $\boldsymbol{d}^{obs}$ before inversion begins. The sensitivity screening identifies which GP-parameters exert the strongest control on the simulated EM responses and therefore which parameter ranges are most relevant when diagnosing a mismatch between the prior-data ensemble and the observations. The subsequent falsification procedure evaluates whether the prior ensemble spans the data-consistent region and, when it does not, uses parameter-colored PCA diagnostics to guide refinement of the prior ranges. This procedure serves a dual purpose: it constrains the prior to a geophysically plausible subspace, and it generates the ensemble of conductivity model–data pairs used to train the surrogate forward model described in Section 3.3.

Starting from broad physically plausible ranges for the GP-parameters, an initial ensemble of parameter vectors is sampled and used to generate 3D conductivity realizations and their corresponding forward EM responses. Distance-based Generalized Sensitivity Analysis (DGSA; Fenwick et al., 2014) is then applied to quantify the relative influence of each GP-parameter on the distance between simulated responses and the observed data. Parameters with high sensitivity scores exert a strong influence on the response amplitude, spatial variation, or temporal decay and are therefore expected to require more careful range specification. Parameters with low sensitivity scores may retain broader prior ranges because the data provide comparatively little information with which to distinguish their values.

DGSA is performed only once using the initial broad prior ensemble. Because its purpose is to identify the relative data sensitivity of the GP-parameters rather than to define their final ranges, it is not repeated during subsequent falsification iterations. The resulting sensitivity ranking is instead used as a diagnostic guide when interpreting parameter-colored PC projections and deciding which ranges should be adjusted.

Following the sensitivity screening, the prior ranges are evaluated and refined through the following procedure:

1. *Broad ranges for each component of* $\boldsymbol{\theta}$ *is specified based on general characteristics of data curve, general geological knowledge, and survey geometry, from which a large ensemble of K GP-parameter vectors* $\{\boldsymbol{\theta}^{(K)}\}_{k=1}^{K}$ *is drawn independently and uniformly;*
2. *For each* $\boldsymbol{\theta}^{(K)}$*, a 3D conductivity realization* $\mathbf{m}^{(K)}$ *is generated by evaluating the Gaussian process, and the corresponding synthetic prior EM data,* $\boldsymbol{d}^{(K)}$*, are computed using the numerical PDE-based forward solver (e.g., SimPEG, Cockett et al., 2015), forming a prior data ensemble;*
3. *We first consider the extent to which the prior data ensemble covers the dynamic range of the* $\boldsymbol{d}^{obs}$*. If prior data ensemble cannot completely encompass the* $\boldsymbol{d}^{obs}$*, the prior is considered falsified at this initial stage, and we roll back to step 1 and start over with adjusted log-mean or -standard deviation of conductivity;*
4. *If prior data ensemble fully covers the* $\boldsymbol{d}^{obs}$*, PCA is then applied to both the observed data and simulated prior data together at each of the time channels, retaining the leading principal components that cumulatively explains 95% of the total data variance;*
5. *Falsification is then assessed by examining whether the projection of* $\boldsymbol{d}^{obs}$ *lies within the cloud of the prior-data ensemble at every selected time channel. To diagnose the source of any mismatch, the ensemble cloud is color-coded according to the value of each GP-parameter. Particular attention is given to parameters identified as sensitive by DGSA. When a sensitive parameter exhibits a clear monotonic pattern in PC space, for example, when progressively higher or lower values systematically shift the prior cloud toward the observed-data projection, the corresponding prior range is shifted, expanded, or contracted in the indicated direction. If the observed projection remains outside the ensemble cloud, the prior fails to capture the signature presented in* $\boldsymbol{d}^{obs}$ *and is considered falsified, and Steps 1–5 are repeated using the revised ranges.*
6. *The procedure is repeated until the prior-data ensemble adequately covers the observed data in both the original response space and the retained PC spaces across all selected time channels. Because the magnitude of the required range adjustment is not available analytically, the range refinement is determined iteratively through repeated forward simulation and diagnostic evaluation.*

This procedure does not optimize a single GP-parameter combination toward the observed data. Rather, it refines the support of the prior so that the ensemble contains a sufficiently broad range of models capable of producing data consistent with the observations. A non-falsified prior does not guarantee the existence of a solution within the specified range; rather, it rejects prior whose sampled prior-predictive responses fail to represent the observations at the adopted diagnostic resolution, providing a principled and data-driven basis for prior elicitation in the absence of geological knowledge. The procedure is therefore termed prior falsification rather than prior verification.

The final non-falsified ensemble $\{\boldsymbol{m}^{(k)}, \boldsymbol{d}^{(K)}\}_{k=1}^{K}$ is retained as training dataset for the surrogate model described in Section 3.3. This ensures that the surrogate is conditioned to operate within the geophysically plausible region of model space relevant to the current dataset being solved.

3.2.1. Prior Falsification with respect to Field Data

The sensitivity-screening and falsification procedure described in Section 3.2 was applied to the field dataset before surrogate training and posterior sampling. An initial broad ensemble of GP-parameter combinations was first generated and evaluated using DGSA to identify which components of $\boldsymbol{\theta}$ most strongly influence the field-data response. Figure 3a shows the resulting sensitivity scores. The mean and standard deviation of log-conductivity are classified as the most influential parameters because they exert the strongest control on the amplitude and temporal decay of the EM response. The roll angle is also identified as important, whereas the major-axis correlation length, aspect ratios, yaw angle, and pitch angle are relatively insensitive at the scale and geometry of the selected survey profile. These results indicate that refinement of the prior should focus primarily on the conductivity mean and standard deviation, while broader ranges may be retained for the weakly sensitive spatial parameters.

Guided by this sensitivity ranking, the prior ranges were refined iteratively using the data-space and parameter-colored PCA diagnostics described in Section 3.2. At each iteration, GP-parameter vectors were sampled from the current ranges, converted into 3D conductivity realizations, and forward modeled. When the observed-data projection was insufficiently covered in PC space, the color-coded ensemble clouds were examined for systematic trends associated with the sensitive GP-parameters. Ranges were then shifted, expanded, or contracted in the direction indicated by those trends, and the forward-modeling and PCA analyses were repeated.

The consistency of the final prior ensemble with the field data $\boldsymbol{d}^{obs}$ was evaluated with two complementary diagnostics. First, Figure 3-b1 through -b4 shows PCA cross plots of the forward-simulated ensemble and $\boldsymbol{d}^{obs}$ (red star) at the earliest (Channel 1) and latest (Channel 12) selected time channels in both PC1–PC2 and PC3–PC4 spaces. The field data projection falls within the ensemble point cloud at all time channels, indicating that the observed diffusion signature is captured within the prior range. Second, Figure 4 shows the prior ensemble of forward-simulated responses (gray curves) overlaid with the observed field data (red curve) across all 12 selected time channels. The observed signal falls within the envelope of simulated responses consistently across all channels, providing direct visual confirmation that the prior is not falsified.

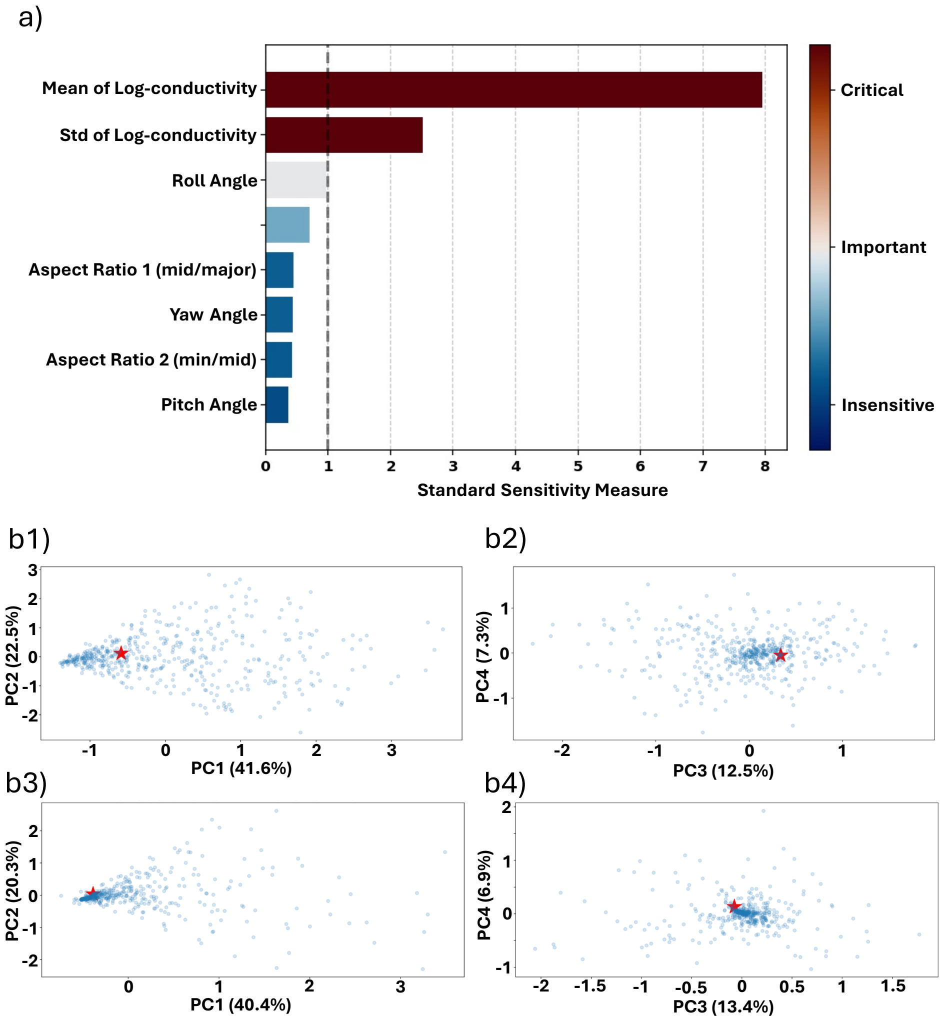

Figure 3. a) Sensitivity test results via DGSA; b) Cross plots of PC scores of field data and cloud of prior at different time channels. The percentage marks how much of data variance explained by the corresponding PC.

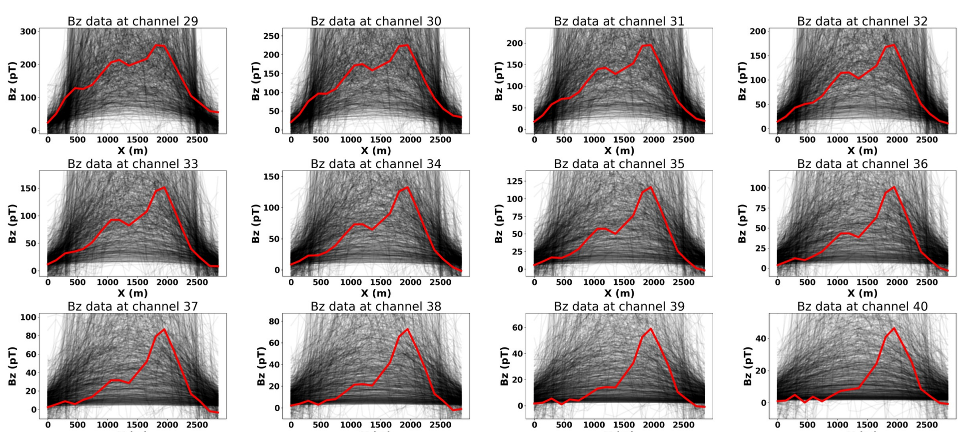

Figure 4. Ensemble of prior data, shown in thin black curves, compared against the true data curve in red at each time channel.

The final non-falsified prior ranges for all eight GP-parameters are summarized in Table 1. The associated non-falsified ensemble of 1000 conductivity realizations and their corresponding forward simulations are subsequently used as training data for the surrogate model described in Section 3.3.

Table 1. Unfalsified GP-parameters, conditioned by field data. U(·) represents uniform distribution.

GP-Parameter	Definition	Prior Uncertainty	Unit
$\boldsymbol{\ell_{maj}}$	Major-axis correlation length	U(1600, 2400)	m
$\boldsymbol{R_{mid/maj}}$	Aspect ratio between major-axis and intermediate-axis correlation lengths	U(0.5, 1.0)	/
$\boldsymbol{R_{min/mid}}$	Aspect ratio intermediate-axis and minor-axis correlation lengths	U(0.3, 1.0)	/
$\boldsymbol{\phi_{yaw}}$	Yaw angle	U(5, 175)	°
$\boldsymbol{\phi_{pitch}}$	Pitch angle	U(-85, 90)	°
$\boldsymbol{\phi_{roll}}$	Roll angle	U(-85, 85)	°
$\boldsymbol{\mu_{\sigma}}$	Mean of conductivity in natural-log scale	U(-2.5, 0.5)	$\ln(S/m)$
$\boldsymbol{s_{\sigma}}$	Standard deviation of conductivity in natural-log scale	U(1.2, 3.5)	$\ln(S/m)$

3.3. Fast Forward Modeling via Deep-Learning Surrogate Model

One of the challenges of McMC sampling is computation. Evaluating the likelihood $p\left(\boldsymbol{d}^{obs}\middle|\boldsymbol{m}\right)$ at every McMC step requires repeated calls to the forward operator $\boldsymbol{\mathcal{F}}(\cdot)$, which involves solving large-scale PDEs describing transient EM difussion. A single forward evaluation on a refined 3D grid can require up to hours of computation, and since McMC likelihood evaluations within a single chain are sequential, it renders direct McMC with the full numerical solver intractable for the tens of thousands of iterations needed for chain convergence. To overcome this bottleneck, we replace $\boldsymbol{\mathcal{F}}(\cdot)$ with a deep-learning surrogate $\widehat{\boldsymbol{\mathcal{F}}}(\cdot)$ that approximates the forward response at a fraction of the computational cost, while retaining sufficient accuracy for likelihood evaluation during McMC.

The surrogate is built on a 3D U-Net architecture (Ronneberger et al., 2015) with an output head added, as shown in Figure 5. This architecture is adapted here for the mapping from a 3D conductivity field to a multi-channel surface EM response. The input to the network is a 3D log-conductivity model $\boldsymbol{m}$ discretized on same voxel grid, $\mathfrak{D}$, used in parameterization that is in the shape of $D_X \times D_Y \times D_Z$ in X-, Y-, and Z-directions, and the output is the predicted TDEM response $\widehat{\boldsymbol{d}} \in \mathbb{R}^{T \times N_{obs}}$ where N_{obs} is the number of surface observation locations along the survey line, and $N = T \times N_{obs}$. The encoder path applies three successive downsampling stages using strided 3D convolutions with instance normalization and dropout, extracting spatial features at progressively coarser scales with channel depths of 32, 64, and 128. A bottleneck block at the deepest level expands the representation to 256 channels. The decoder path mirrors the encoder through interpolation-based upsampling followed by $1 \times 1 \times 1$ convolutions, with skip connections from corresponding encoder levels, recovering spatial resolution while preserving multiscale features. In this work, the spatial dimensions along the $Y-$ and $Z-$directions are collapsed following decoding through a learned YZ squeeze operation, implemented as a channel-wise convolution over the $Y-$ and Z -directions, yielding a 1D feature sequence along the $X-$ direction, which is then resampled to the N_{obs} observation locations via linear interpolation. A final 1D convolutional head maps the feature sequence to the T time channel outputs. The resulting network contains 5,882,892 trainable parameters.

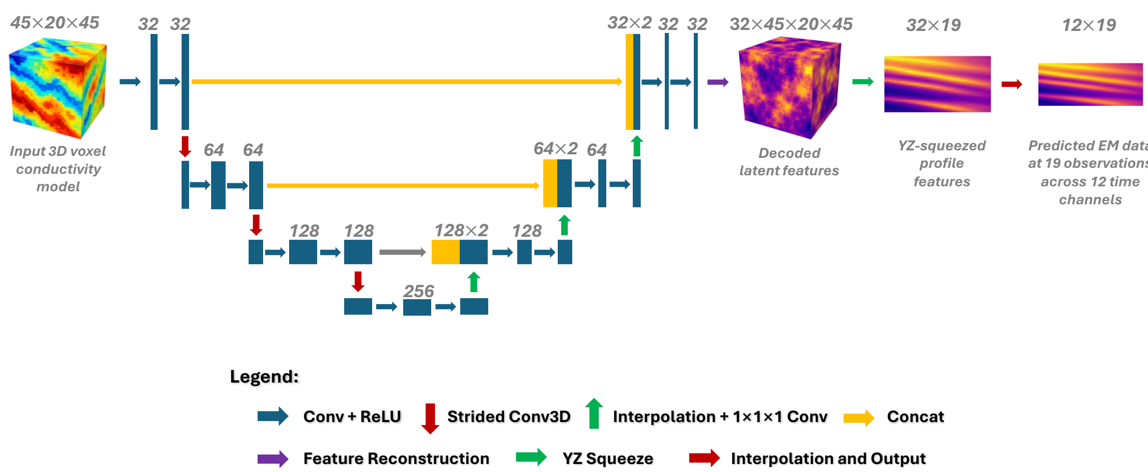

Figure 5. Diagram of U-Net based surrogate model for fast EM forward modeling used in this work.

Training data are provided directly by the non-falsified ensemble generated during the falsification step described in Section 3.2. The 1,000 clean model–data pairs are first partitioned into training (800), validation (150), and test (50) splits on the clean realizations; augmentation is then applied exclusively to the training split by adding independent Gaussian noise drawn uniformly from [0%, 10%] of the mean absolute amplitude of each time channel, producing seven additional noisy copies per sample and yielding 6,400 training pairs in total. The network is trained with a batch size of 64 using the Adam optimizer (Kingma and Ba, 2014) with a learning rate initialized at 10^{-3} and reduced by a factor of 0.5 whenever the validation loss plateaus, and training is terminated by early stopping based on validation loss, with a maximum of 1,000 epochs.

A standard Mean Square Error (MSE) loss is poorly suited to TDEM data because the signal amplitude decays by several orders of magnitude across time channels, causing the loss to be dominated by the early-time channels with the largest dynamic range (DR). To address this, we employ a dynamic-range-weighted MSE loss that normalizes the squared prediction error in each time channel by the squared dynamic range of that channel in the target data,

$$\mathcal{L}_{DR} = \frac{1}{B \cdot T} \sum_{b=1}^{B} \sum_{t=1}^{T} \frac{1}{{\Delta_t^{(b)}}^2} \sum_{n=1}^{N_{obs}} \left(\hat{d}_{b,t,n} - d_{b,t,n}^{obs} \right)^2, \tag{5}$$

where B is the batch size. The quantity $\Delta_t^{(b)}$ is the dynamic range of time channel t for sample b in the batch, clamped below at 10^{-12} to avoid division by zero, and it is defined as

$$\Delta_t^{(b)} = max_n(d_{b,t,n}^{obs}) - min_n(d_{b,t,n}^{obs}). \tag{6}$$

This weighting ensures that late-time channels, which carry information about deeper structure but have smaller absolute amplitudes, contribute comparably to the loss as early-time channels, promoting accurate surrogate approximation across the full decay curve.

3.3.1. Surrogate Model Validation

Before deployment within the McMC sampler, the trained surrogate is evaluated on the 50 held-out test models, which were excluded from both training and noise augmentation. Training converged after approximately 595 epochs, at which point the dynamic-range-weighted validation loss had decreased from 242.5 at initialization to approximately 3.0 (Figure 6). The lower validation loss relative to the training loss is attributable to the training configuration: dropout is active and the training responses are noise-augmented, whereas validation is performed with dropout disabled on clean samples. The training and validation curves therefore reflect different effective prediction conditions.

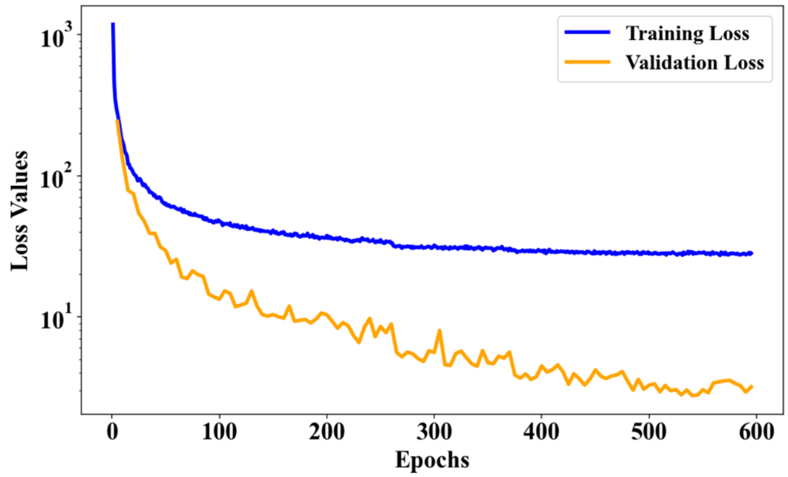

Figure 6. Loss curve of training the surrogate model.

On the held-out test set, the surrogate achieves a dynamic-range-weighted MSE of 2.35. To provide a scale-independent measure of prediction accuracy that is comparable across samples with different response amplitudes, we additionally compute the normalized MSE (NMSE) for each test sample, defined as the per-sample MSE divided by the variance of the corresponding target response across all time channels and observation locations. A NMSE of zero indicates perfect prediction, while a value of one corresponds to a predictor no better than the sample mean. The surrogate attains a mean NMSE of 0.83% (standard deviation 1.30%) across the 50 test samples, ranging from 0.05% in the best case to 8.25% in the worst, indicating that the surrogate predictions account for most of the response variance on average. The close agreement between predicted and target response statistics confirms that the surrogate reproduces both the amplitude and dynamic range of the multi-channel TDEM response with low bias.

Figure 7 shows surrogate predictions against true PDE-simulated responses for nine randomly selected test samples across all 12 time channels. The predicted curves closely track the true responses in both amplitude and decay shape across the whole time range, confirming that the surrogate generalizes well within the non-falsified prior range.

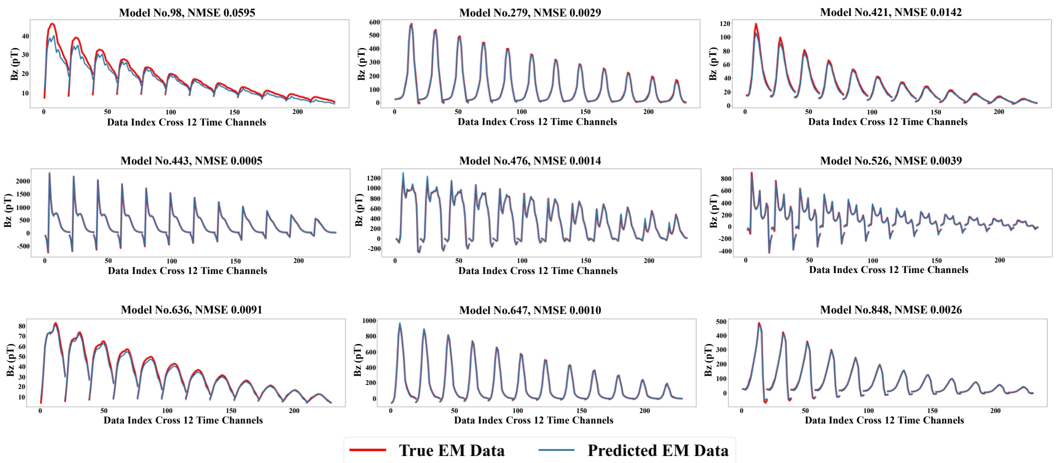

Figure 7. Comparison between truth EM data calculated with PDE solver and surrogate model prediction. All 12 time channels are concatenated into one curve for each test example.

This validation is by design in-distribution that the surrogate is trained and evaluated on GP realizations drawn from the non-falsified prior, which defines the exact model space where the following inversion operates. Prior falsification in Section 3.2 ensures that this space covers the data-consistent region before inversion begins, so the surrogate operates within its validated range throughout posterior sampling. The extent to which this guarantee holds for subsurface structures that deviate from the GP prior assumption is addressed through the prior-misspecification synthetic tests in Section 4.2.

3.4. Random Walk via Probability Perturbation Method (PPM)

With the surrogate $\widehat{\boldsymbol{\mathcal{F}}}(\cdot)$ in place for the forward modeling, the McMC sampling of the joint posterior $p\left(\boldsymbol{m},\boldsymbol{\theta}\middle|\boldsymbol{d}^{obs}\right)$ requires a random walk that perturbs both the GP-parameters $\boldsymbol{\theta}$ and the high-dimensional 3D conductivity field $\boldsymbol{m}$ simultaneously. A naive pixel-based random walk perturbing individual voxel values directly is geologically unrealistic and statistically inefficient, as independent perturbations destroy the spatial continuity encoded by the Gaussian process prior. The Probability Perturbation Method (PPM, Caers, 2003; Caers and Hoffman, 2006) addresses this by perturbing the underlying uniform random vectors that generate $\boldsymbol{m}$ through the prior's generative mapping, rather than perturbing $\boldsymbol{m}$ directly. This ensures that the latent variables remain distributed according to their reference priors and that the resulting conductivity realization is generated through the GP model associated with the proposed hyperparameters, preserving geological realism and prior consistency throughout the chain. Here, we revisit the explanation of this method that was provided by Caers and Hoffman (2006).

To build intuition, consider first the simplest case: generating correlated draws of a Bernoulli random variable x with probability p. An independent draw is obtained as

$$u \sim Uniform(0,1);\;\; if(u \leq p)\; x = 1, else\; x = 0. \tag{7}$$

To generate a correlated sequence $\{x_i\}$ that preserves the marginal probability p, the next draw is sampled using a perturbed probability:

$$p_{perturbed} = rp + (1-r)x_{i-1}, \tag{8}$$

where $r \in [0, 1]$ controls the degree of serial correlation: $r = 1$ yields a fully independent new draw, while $r = 0$ reproduces the previous draw exactly. Critically, the expectation of the perturbed draw is preserved regardless of r:

$$E[x_i = 1] = rp + (1-r)E[x_{i-1} = 1] = p. \tag{9}$$

This expectation-preservation property is the foundation on which PPM proposals remain compatible with standard Metropolis-Hastings sampling in McMC, because the perturbed draw is marginally distributed according to the same prior as the unperturbed draw, the proposal transition kernel is symmetric,

$$q(\boldsymbol{\theta}'|\boldsymbol{\theta}) = q(\boldsymbol{\theta}|\boldsymbol{\theta}'), \tag{10}$$

where $\boldsymbol{\theta}'$ is the new proposal, and no additional proposal-ratio correction is required in the acceptance probability described in Section 3.5.

This framework extends to any univariate distribution with cumulative distribution function (CDF) $\boldsymbol{\mathcal{G}}(\cdot)$ and quantile function $\boldsymbol{\mathcal{G}}^{-1}(\cdot)$ by replacing p with $\boldsymbol{\mathcal{G}}(u)$. The perturbed CDF is defined as

$$\boldsymbol{\mathcal{G}}_{perturbed}(u, r, u_0) = (1-r)1_{u>u_0} + r\boldsymbol{\mathcal{G}}(u), \tag{11}$$

and the corresponding perturbed draw,

$$u_r = PPM(u_0, r, u_1), \tag{12}$$

for a new independent draw $u_1 \sim Uniform(0,1)$ is given by the piecewise expression:

$$\boldsymbol{u_r = PPM(u_0, r, u_1) = \begin{cases} u_1/r & if\; u_1 \leq ru \\ u_0 & if\; ru_0 < u_1 < 1 - r + ru_0 \\ (u_1 + r - 1)/r & if\; u_1 \geq 1 - r + ru_0 \end{cases}} \tag{13}$$

As in the Bernoulli case, u_r remains marginally $Uniform(0,1)$ for any r, and model parameters are recovered via

$$\theta = \boldsymbol{\mathcal{G}}^{-1}(u_r), \tag{14}$$

ensuring proposed values remain within the prior support by construction.

Equation 13 defines PPM for a single scalar probability. For a random vector, we apply the same scalar transformation element-wise in the underlying uniform probability space. Let

$$\boldsymbol{u}_0 = (u_{0_1}, u_{0_2}, \ldots, u_{0_M}) \tag{15}$$

denote an M-dimensional uniform random vector, and let

$$\boldsymbol{u}_1 = (u_{1_1}, u_{1_2}, \ldots, u_{1_M}) \tag{16}$$

be an independently generated auxiliary vector of the same dimension, whose elements follow uniform distribution between 0 and 1. The perturbed vector is obtained as

$$u_{r_m} = PPM(\boldsymbol{u}_{0_m}, r, \boldsymbol{u}_{1_m}), \qquad m = 1, 2, \ldots, M, \tag{17}$$

Or equivalently,

$$\boldsymbol{u}_r = PPM(\boldsymbol{u}_0, r, \boldsymbol{u}_1), \tag{18}$$

where the operator on the right-hand side is understood to act element-wise. Each component receives an independent auxiliary perturbation u_{1_m}, whereas the same r is shared by all components within a parameter group and controls the overall perturbation strength. Because both the reference uniform distribution and the PPM transformation factorize by component, the perturbed vector retains the independent multivariate uniform reference distribution. This component-wise construction is used below for both the latent voxel field and the vectors of GP-parameters.

Figure 8 shows an example of how different r values perturb the spatial pattern of a 2D Gaussian random field through PPM: from realization 1 to 9, the r value increase from 0 to 1, and the first few realizations are similar to realization 1 with only nuances. With increased r, the later realizations gradually become more distinct and finally an individual draw. Thus, the element-wise perturbation does not imply that the resulting conductivity voxels are spatially independent; spatial dependence is imposed subsequently through the Gaussian-process covariance transformation.

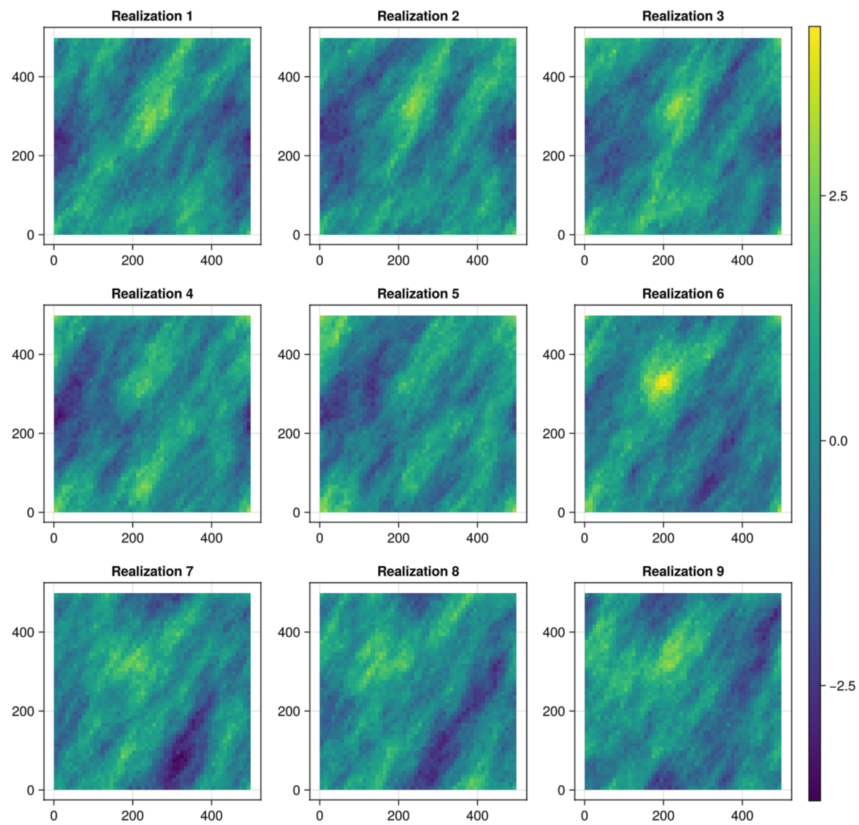

Figure 8. A 2D example showing how PPM perturb a field (courtesy of Caers et al., 2026). Geometry is fixed, and only spatial pattern is perturbed. From realizations 1 to 9, the r increases from 0 to 1.

In our implementation, four parameter groups are perturbed simultaneously and independently within each proposal:

1. $\boldsymbol{u}^{field}$ for latent random field $\boldsymbol{w}$ on the full 3D voxel grid $\mathfrak{D}$;
2. $\boldsymbol{u}^{aniso}$ for six anisotropy parameters (spatial correlation ranges, aspect ratios, and orientation angles);
3. $\boldsymbol{u}^{mean}$ for the log-conductivity mean;
4. and $\boldsymbol{u}^{std}$ for the log-conductivity standard deviation,

each with its own perturbation parameter r_j, where $j = \{field, aniso, mean, std\}$:

$$\boldsymbol{u}_r^j = PPM(\boldsymbol{u}_0^j, r_j, \boldsymbol{u}_1^j). \tag{19}$$

Because the field's generative distribution is conditioned on the GP-parameters $\boldsymbol{\theta}$, the perturbed GP-parameters,

$$\boldsymbol{\theta}_r \leftarrow \mathcal{G}^{-1}\left(\boldsymbol{u}_r^{aniso,mean,std}\right), \tag{20}$$

are reconstructed first, and the perturbed field vector $\boldsymbol{u}^{field}$ is then mapped through the latent Gaussian variable and Fast Fourier Transform (FFT) -based simulation to produce a new conductivity realization $\boldsymbol{m}_r$ consistent with $\boldsymbol{\theta}_r$. This ordering reflects a computational dependency in constructing the joint proposal $(\boldsymbol{m}, \boldsymbol{\theta})$, while all four perturbations occur within a single McMC step rather than as a sequential or alternating sampling scheme. By perturbing all parameter groups jointly, the random walk avoids becoming trapped in local optima associated with any single group, while the independent r_j values allow perturbation strength (step length) to be tuned separately for the low-dimensional covariance structure and the high-dimensional spatial field. The specific values of r_j and their annealing schedule are described in Section 3.6 in the context of the delayed rejection sampler.

3.5. Extended Metropolis-Hastings Sampler with Delayed Rejection

With the PPM-based random walk defined in Section 3.4, posterior sampling proceeds via the Metropolis-Hastings (MH) algorithm (Metropolis et al., 1953; Hastings, 1970). At each iteration i, a joint proposal $(\boldsymbol{m}_r, \boldsymbol{\theta}_r)$, is generated by applying PPM to the current state, $(\boldsymbol{m}_i, \boldsymbol{\theta}_i)$, and the surrogate forward response,

$$\widehat{\boldsymbol{d}}_{\boldsymbol{r}} = \widehat{\boldsymbol{\mathcal{F}}}(\boldsymbol{m}_{\boldsymbol{r}}), \tag{21}$$

is evaluated. The data misfit at each McMC state is quantified by a noise- and dynamic-range-weighted mean squared error loss:

$$\boldsymbol{\mathcal{L}}(\boldsymbol{m}) = \frac{\mathbf{1}}{\boldsymbol{T}} \sum_{t=1}^{T} \frac{\boldsymbol{\omega}_t^2}{\boldsymbol{N}_{\boldsymbol{obs}}} \sum_{n=1}^{N_{obs}} \left(\frac{\hat{\boldsymbol{d}}_{t,n} - \boldsymbol{d}_{t,n}^{obs}}{\boldsymbol{\sigma}_{t,n}} \right)^2, \tag{22}$$

Where $\omega_t = 1/\Delta_t$ is the inverse of dynamic range weight for time channel t, and $\sigma_{t,n}$ is the standard deviation of the measurement noise at observation location n and time channel t. This loss extends the dynamic-range weighting used for surrogate training (Equation 4) by additionally normalizing residuals by the data noise, ensuring that noisier observations contribute proportionally less to the misfit. The two loss functions serve distinct purposes: the surrogate training loss promotes accurate approximation across all time channels on clean numerical simulations, while the McMC loss evaluates consistency between surrogate predictions and noisy field observations in a noise-aware manner.

The proposal is accepted or rejected according to a Metropolis acceptance probability tempered by a positive temperature parameter τ,

$$\alpha(\boldsymbol{m}_r, \boldsymbol{m}_i) = \min\left\{1, \exp\left(-\frac{\mathcal{L}_r(\boldsymbol{m}_r) - \mathcal{L}_i(\boldsymbol{m}_i)}{\tau}\right)\right\}, \tag{23}$$

where $\mathcal{L}_i$ and $\mathcal{L}_r$ are the losses at the current and proposed states, respectively. This tempered formulation shares the Metropolis criterion with simulated annealing (Kirkpatrick et al., 1983) and controls the acceptance threshold through the temperature parameter τ rather than fixing it to a single noise variance estimate, which provides greater flexibility in navigating the loss landscape during early chain exploration. Because PPM proposals are marginally distributed according to the same prior as the current state, the proposal transition kernel is symmetric, and no additional proposal-ratio correction is required in the acceptance probability.

A practical challenge in applying PPM within MH sampling is the choice of the perturbation parameters r_j, which effectively control step length at each random walk. A value of r_j close to 1 produces large, nearly independent proposals that explore the prior broadly but are frequently rejected; a value close to 0 produces highly correlated proposals that are accepted more readily but mix slowly. Rather than fixing r_j to a single value throughout, we adopt a two-stage delayed rejection strategy (Tierney and Mira, 1999; Green and Mira, 2001) combined with an annealing schedule for the Stage-2 perturbation strength, balancing global exploration and local refinement within each iteration. In this design, each McMC iteration proceeds in a two-stage manner as follows:

1. A Stage-1 proposal is first generated using perturbation parameters $r_{j_{large}} \sim Uniform(0.8, 1)$ applied independently to all four parameter groups. This large perturbation produces a proposal that is nearly an independent draw from the prior, allowing the chain to escape local optima and explore the full prior support. The Stage-1 acceptance probability is

$$\alpha_1\left(\mathbf{m}_{r_1}, \boldsymbol{m}_i\right) = \min\left\{1, \exp\left(-\frac{\mathcal{L}_{r_1}\left(\mathbf{m}_{r_1}\right) - \mathcal{L}_i(\boldsymbol{m}_i)}{\tau}\right)\right\}, \tag{24}$$

2. If Stage-1 is accepted, the chain proceeds to next iteration. If Stage-1 is rejected, a Stage-2 proposal is generated from the current state using smaller perturbation parameters $r_{j_{small}} \sim Uniform(0, r_{j_{annealed}})$, producing a more conservative local refinement. To preserve detailed balance and ensure samples are drawn from the correct target distribution, the Stage-2 acceptance probability includes a correction term accounting for the failed Stage-1 transition:

$$\alpha_2\left(\mathbf{m}_{r_1}, \mathbf{m}_{r_2}, \boldsymbol{m}_i\right) = \min\left\{1, \exp\left(-\frac{\mathcal{L}_{r_2}\left(\mathbf{m}_{r_2}\right) - \mathcal{L}_i(\boldsymbol{m}_i)}{\tau}\right) \cdot \frac{1 - \alpha_1\left(\mathbf{m}_{r_2}, \mathbf{m}_{r_1}\right)}{1 - \alpha_1\left(\boldsymbol{m}_i, \mathbf{m}_{r_1}\right)}\right\}, \tag{25}$$

The correction ratio accounts for the probability that Stage 1 would have been rejected had the chain originated from the Stage-2 proposed state $(\boldsymbol{m}_{r_2}, \boldsymbol{\theta}_{r_2})$ rather than the current state $(\boldsymbol{m}_i, \boldsymbol{\theta}_i)$, which is necessary to maintain ergodicity. The evolution of $r_{j_{small}}$ over the chain and their values are described in following sections.

3.6. Adaptive Annealing of Perturbation Parameters and Sampling Temperature

The delayed rejection sampler described in Section 3.5 requires the specification of two sets of tuning parameters that govern the chain's behavior: the Stage-2 perturbation parameters, $r_{j_{small}}$, controlling proposal aggressiveness, and the temperature τ controlling acceptance sensitivity. Rather than fixing these parameters to constant values throughout the chain, we adopt an adaptive annealing strategy that evolves both over the course of sampling, progressively transitioning the chain from broad prior exploration in early iterations to fine-grained posterior characterization in later iterations (Kirkpatrick et al., 1983).

The perturbations $r_{j_{large}}$ in Stage-1 are sampled randomly from a distribution of higher value range throughout the entire chain, ensuring the sampler retains its ability to make large exploratory jumps regardless of chain progress. Only the perturbations $r_{j_{small}}$ in Stage-2 are sampled randomly from tighter value ranges subject to annealed upper-bounds $r_{j_{annealed}}$, evolving according to an exponential decay schedule:

$$r_{j_{annealed}}(t) = r_{j_{min}} + \left(r_{max} - r_{j_{min}}\right) exp\left(-\lambda_j \iota\right) \tag{26}$$

where $\iota \in [0, 1]$ is the normalized iteration index within the annealing period (ρ_{anneal}), $r_{max} = 1$, whereas $r_{j_{min}}$ and λ_j are the group-specific minimum perturbation radius and decay rate, respectively. As aforementioned in section 3.4, the perturbations of voxel conductivity model and GP-parameters are handled by total of four uniform random vectors. Thus, four perturbation parameters are needed with distinct $r_{j_{min}}$ and λ_j values, together with parameters controlling lengths of burn-in (ρ_{burn}) and annealing periods, reflecting their different roles and dimensionalities in the inversion. We will discuss the selection of those annealing parameters in following section.

The general design is to have $r_{j_{small}} \sim Uniform(r_{j_{min}}, r_{j_{annealed}})$, whereas the annealing of $r_{j_{annealed}}$ is scheduled in three phases, defined as fractions of the predefined total chain length, $N_{\max}$. During the burn-in phase, the $r_{j_{annealed}}$ are held at $r_{max} = 1$, so that Stage-2 proposals could be as broad as Stage-1, allowing aggressive exploration of the prior before any annealing begins. After burn-in, the annealing begins, and the $r_{j_{annealed}}$ decay exponentially toward $r_{j_{min}}$ for each group independently at each step, progressively concentrating Stage-2 proposals around the current state as the chain converges toward the posterior. In the sampling phase after annealing, the $r_{j_{annealed}}$ are held fixed at $r_{j_{min}}$, enabling fine-grained posterior characterization while Stage-1 continues to attempt large exploratory jumps, which are almost always rejected at this stage but prevent the chain from becoming trapped in a local region of the posterior. This asymmetry between Stage-1 and Stage-2 is deliberate that Stage-1 preserves global ergodicity throughout, while the annealed Stage-2 progressively refines the posterior characterization as the chain matures.

The temperature τ is annealed as chain evolves. It is initialized as $\tau_0 = 10\mathcal{L}_0$, where $\mathcal{L}_0$ is the McMC loss evaluated at the initial state. This initialization ensures that the early chain is sufficiently permissive to accept proposals that worsen the loss, facilitating broad exploration before the sampler begins to concentrate on low-loss regions. Over the course of the chain, τ is adaptively updated every 50 iterations via a Robbins-Monro stochastic approximation scheme (Robbins and Monro, 1951) targeting a nominal acceptance rate of $\alpha *= 0.23$. The update is performed in log-space to ensure positivity and smooth adaptation across orders of magnitude:

$$\log \tau_{i+1} = \log \tau_i + \eta_i(\alpha * - \overline{\alpha}_i) \tag{27}$$

where $\overline{\alpha}_i$ is the empirical acceptance rate computed over a sliding window of the most recent 100 iterations, and η_i the adaptation speed. To ensure convergence of the adaptive scheme, η_i is held constant at η_0 during the burn-in phase and then decayed linearly to zero in log-space over the remainder of the chain:

$$\eta_i = \begin{cases} \eta_0 & \text{if burn-in} \\ \eta_0 \left(1 - \dfrac{i - \rho_{burn} \cdot N_{max}}{(1 - \rho_{burn}) \cdot N_{max}}\right) & \text{if post burn-in} \end{cases}. \tag{28}$$

After updating, the temperature is recovered via exponentiation after each update for weighting. This decay ensures that the temperature τ stabilizes as the chain enters the sampling phase, preventing the adaptive mechanism from destabilizing a chain that has already converged. The target acceptance rate of $\alpha *= 0.23$ is motivated by theoretical results for optimal MH sampling in high-dimensional spaces (Gelman et al., 1997), which suggest acceptance rates in the range of 0.2–0.3 are near-optimal for mixing efficiency.

4. Synthetic Cases

Validating a probabilistic inversion framework requires more than demonstrating that the posterior mean resembles the true model. A rigorous evaluation must address three distinct questions: whether the sampler correctly characterizes the posterior when the prior is well-specified, whether the recovered uncertainty is meaningful when the true model violates the prior assumptions, and whether the method's behavior is stable across a range of tuning parameter choices. These questions are not merely academic. In field applications, the prior is never perfectly specified, tuning parameters must be set without ground truth, and the posterior ensemble rather than any single model is the primary deliverable. The synthetic tests presented in this section are designed to address each of these questions in turn, using cases of increasing difficulty and progressively larger violations of the Gaussian prior assumption, building toward an honest characterization of both the capabilities and limitations of the proposed framework.

4.1. Sensitivity Analysis and Selection of Annealing Parameters

Before running specific test, we need to ensure that posterior results are reliable and reproducible, which requires that the sampler's behavior does not depend critically on the specific values of the annealing parameters introduced in Section 3.6, which must be set a priori and immune from the change of data set to be solved. It is therefore important to establish both whether annealing is necessary for correct posterior recovery and how sensitive the results are to the specific values chosen. We address these two questions in turn using 33 McMC runs on the same synthetic Gaussian true model as Section 4.2, with annealing parameters randomly drawn by Latin Hypercube Sampling (LHS, McKay et al., 2000) across a wide range of plausible values, as shown in Table 3. Among these 33 sensitivity tests, the first three runs disable annealing entirely, holding $r_{j_{annealed}}$ fixed at r_{max} throughout, serving as non-annealing control cases, while the remaining 30 runs use different annealing configurations sampled by LHS. All other aspects of the framework are held fixed across runs.

Table 2. Definition and sampling ranges of six annealing parameters in the LHS sensitivity study.

Annealing Parameter	Definition	Value Range
ρ_{burn}	Burn-in phase length, as a fraction of total chain length	[0.01, 0.30]
ρ_{anneal}	Annealing phase length after burn-in, as a fraction of total chain length	[0.01, 0.50]
λ_{field}	Exponential decay rate of $r_{annealed}$ for the voxel conductivity model	[1.5, 5.0]
$\lambda_{aniso,mean,std}$	Exponential decay rate of $r_{annealed}$ for the GP-parameters	[2.0, 6.0]
$r_{field_{min}}$	Minimum perturbation radius for the voxel conductivity model	[0.05, 0.20]
$r_{aniso,mean,std_{min}}$	Minimum perturbation radius for GP-parameters	[0.05, 0.40]

Figure 9 shows the convergence destination of each run projected onto the space of two most data-sensitive GP-parameters, which are the mean values of mean posterior conductivity and mean standard deviation of posterior conductivity. The 30 annealed LHS runs cluster consistently in a region of parameter space relatively closer to the ground truth. Although their posterior means do not coincide exactly with the true values, their posterior uncertainty bounds are sufficiently broad to cover the ground truth. In contrast, the non-annealing control runs converge to posteriors whose uncertainty bounds fail to cover the ground truth, especially for the mean posterior conductivity that is the most data-sensitive GP-parameter, indicating that the chains have become trapped in local regions of parameter space inconsistent with the true model. This result demonstrates that annealing is a necessary for correct posterior recovery. Without a progressive reduction in perturbation strength (step length), the samplers fail to maintain sufficient posterior uncertainty to capture the true parameter values, even when the posterior mean appears broadly reasonable.

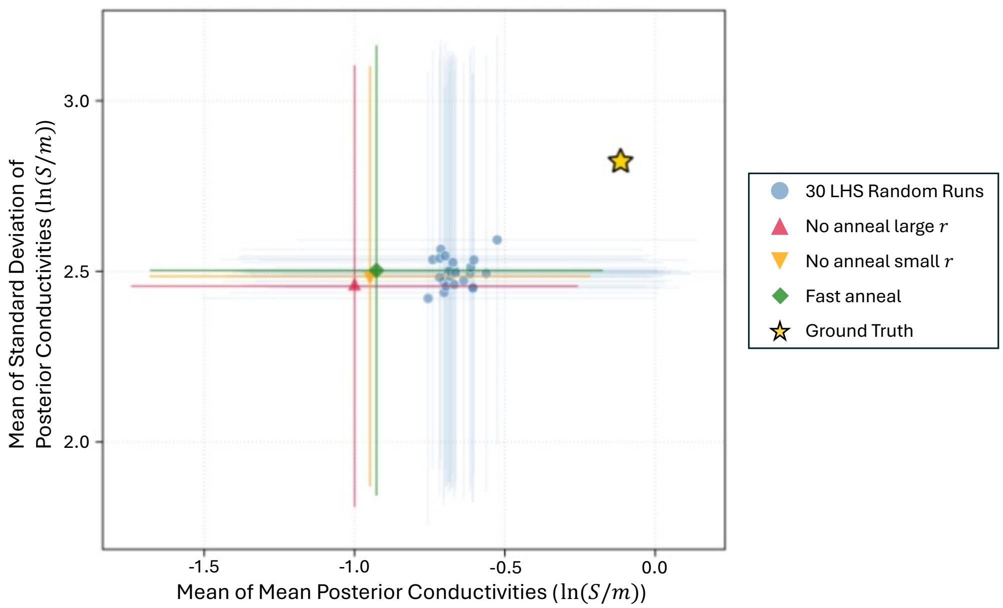

Figure 9. Convergence destination in GP-parameter space for all sensitivity tests. Scatters denote values of each run, and bars indicate uncertainty bounds. Here we only examine the destinations against most data-sensitive GP-parameters.

Having established the necessity of annealing, we turn to the question of how sensitive the results are to the specific annealing parameter values within the annealed runs. The cluster of 30 annealed runs shown in Figure 9 tell that different annealing parameters tends to lead the chain to the similar end point. To quantify the influence of annealing parameter choice on posterior results, we compute the within-run posterior uncertainty to the cross-run variability of posterior means. The mean of posterior standard deviation within runs, which explains the total uncertainty, is 2.6044, whereas the standard deviation of posterior means across runs, which explains the sensitivity, is 0.1468. Taking the ratio of these two matrices gives us the contribution of choices of different annealing parameters to the total posterior uncertainty, which it's 5%. This indicates that different choices of annealing strategy contribute only a minor fraction of uncertainty.

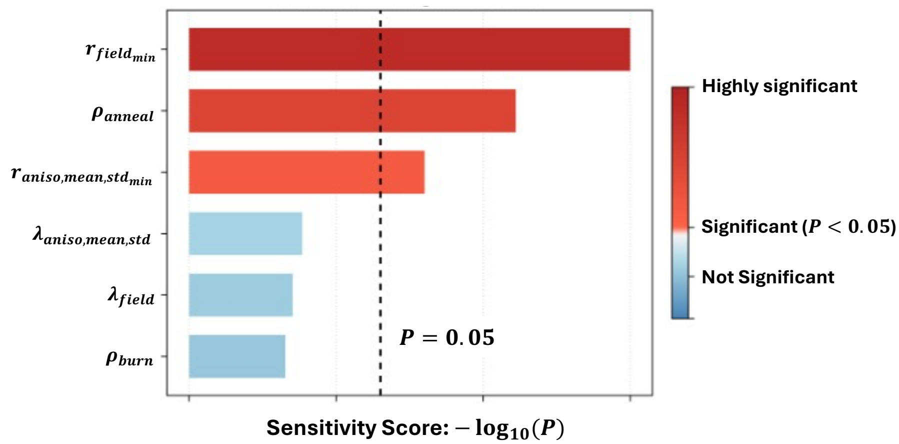

Figure 10. Permutation-based sensitivity analysis of chain convergence with respect to different annealing parameters.

To identify which specific annealing parameters most influence convergence, Figure 10 shows a permutation-based sensitivity analysis quantifying the influence of each annealing parameter on chain convergence. The three parameters with scores exceeding the $P = 0.05$ significance threshold are $r_{field_{min}}$, ρ_{anneal}, and $r_{aniso,mean,std_{min}}$, indicating that the minimum perturbation radii and the annealing period length have the most statistically significant influence on convergence quality. In contrast, the decay rates and the burn-in ratio are not as significant and can be set relatively freely without substantially affecting convergence. Based on these findings and loss values from 30 LHS runs, we fix the annealing parameters to the values listed in Table 3 for all subsequent synthetic and field tests. The voxel conductivity model realization is assigned with a larger minimum radius and slower decay rate than the GP-parameters. This is in consideration that the field is high-dimensional and perturbations at very small r produce negligible changes in the forward EM response, which would effectively freeze the chain.

Table 3. Annealing parameters chosen for tests in this work.

Annealing Parameter	Value
ρ_{burn}	0.2
ρ_{anneal}	0.3
λ_{field}	3.0
$\lambda_{aniso,mean,std}$	4.0
$r_{field_{min}}$	0.3
$r_{aniso,mean,std_{min}}$	0.1

4.2. Synthetic Test: Gaussian True Model

In this test, the true conductivity model $\boldsymbol{m}^{true}$ is one of realizations of the Gaussian process with a known covariance structure, drawn from the non-falsified prior ensemble. Specifically, it is selected from a held-out test set that used for testing after surrogate model training. The GP-parameters controlling the covariance are treated as unknown to the sampler, and the framework is tasked with jointly recovering both the 3D conductivity field and the GP-parameters from the synthetic observed data $\boldsymbol{d}^{obs} = \boldsymbol{\mathcal{F}}(\boldsymbol{m}^{true}) + \boldsymbol{\varepsilon}$. Since the true model is consistent with the prior by construction, this test evaluates the method under ideal prior specification and establishes a baseline for subsequent prior-misspecification tests.

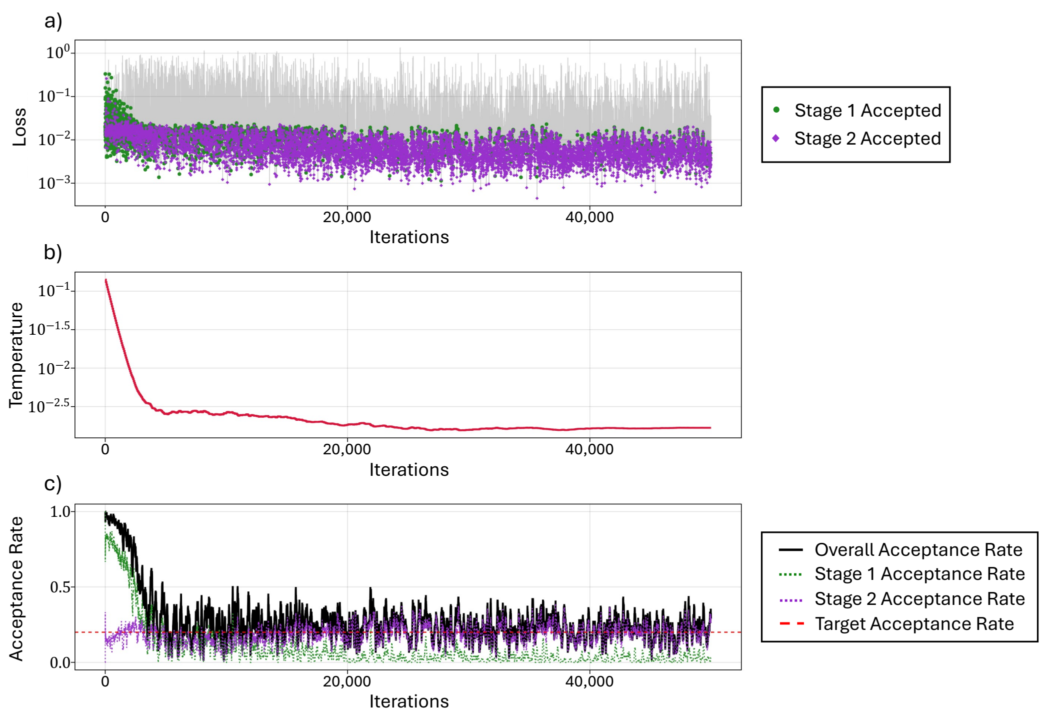

Figure 11. Convergence diagnosis plots of McMC for synthetic test on Gaussian true model. a) Loss curve in log-10 scale, with gray dots representing all proposals, and green and purple dots indicate stage-wise acceptance; b) Temperature curve in log-10 scale; c) Moving-average acceptance rate over a sliding window of 100 iterations.

The McMC chain was run for 50,000 iterations. The total run time for this chain is approximately 3 hours on Apple M4 Pro chip (24 GB unified RAM). Because the delayed rejection sampler performs an additional forward evaluation for rejected first-stage proposals, the complete chain of this test required a total 95,499 forward evaluations. In comparison, a single traditional PDE-based forward evaluation requires approximately 20 minutes for the same problem setup. Completing the equivalent inversion without surrogate acceleration would therefore require approximately 3.6 years of computation, corresponding to a speed-up of more than 10^4X. This acceleration transforms large-scale 3D probabilistic EM inversion from a computationally prohibitive problem into a feasible workflow. After 10,000 iterations of burn-in and

15,000 iterations of annealing, posterior samples are collected from the final 25,000 iterations, or final 50% of the chain. Figure 11 shows the convergence diagnostics for this chain. The weighted MSE loss decreases rapidly during the first 5,000 iterations and stabilizes in the range of 10^{-2} to 10^{-3}, with Stage-2 proposals consistently achieving lower losses than Stage-1 proposals, confirming that the delayed rejection mechanism is functioning as intended. The sampling temperature τ decays smoothly from its initial value and stabilizes around $10^{-2.5}$, while the overall acceptance rate converges to the target of 0.23 after an initial burn-in transient, indicating that the Robbins-Monro adaptation has successfully tuned the sampler.

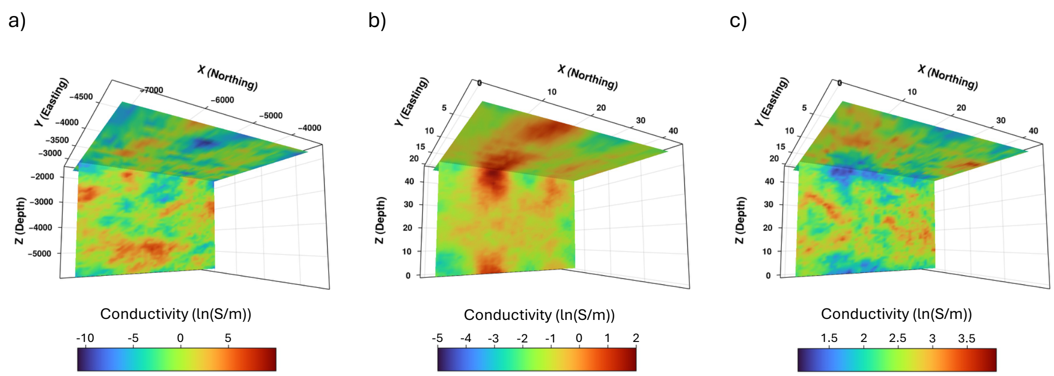

Figure 12. Posterior recovery for the synthetic Gaussian true model test. a) Slices of true conductivity model; b) Slices of mean posterior conductivity model; and c) Standard deviation of posterior conductivity model. All models' values are shown in natural log scale. The posterior mean is reflecting the cancellation of spatially variable features across diverse posterior realizations; the posterior standard deviation is broadly elevated across the domain with slightly higher values at depth, consistent with the limited resolution of surface EM data at greater depths.

Figure 12 shows the true conductivity model, the posterior mean, and the posterior standard deviation. Due to the use of Gaussian Process, the true model is spatially complex, exhibiting scattered conductivity highs and lows distributed across the full 3D volume. The posterior mean is considerably smoother than the true model and does not reproduce individual local features. Instead, it reflects a broad conductivity-high in the shallow upper-left region and a subdued response elsewhere. This near-uniform appearance of the posterior mean is not a failure of the sampler but an expected consequence of ensemble averaging. When the true model contains many spatially distinct features, different posterior realizations recover different subsets of those features, and their average cancels the local variability. This interpretation is confirmed by Figure 13, which shows a few individual posterior realizations where each is spatially complex and geologically plausible, yet no two are alike, demonstrating that the chain is genuinely exploring a diverse family of data-consistent models rather than collapsing to a single solution. The posterior standard deviation is broadly elevated across the domain, with slightly higher values at depth, reflecting the inherently limited resolution of surface EM data at greater depths.

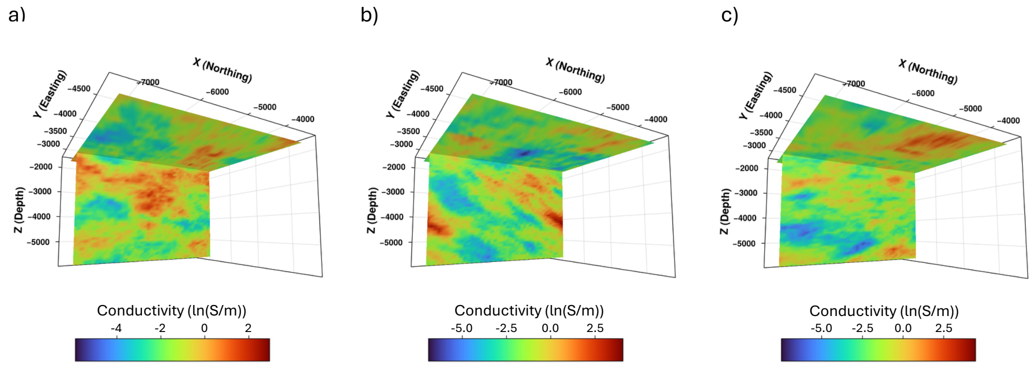

Figure 13. A few realizations of posterior conductivity models. Model values are presented in natural log scale. Although different realization s showing distinct spatial patterns and correlations, they all fit true data to the similar quality.

The posterior data fit is shown in Figure 14. The ensemble of surrogate-predicted responses (black curves) envelops the synthetic observed data (red dots with error bars) consistently across all 12 time channels, confirming that the posterior models are collectively data-consistent. The tight clustering of ensemble responses around the observed signal, particularly at early time channels where the SNR is highest, indicates that the sampler has successfully constrained the forward response despite the high-dimensional and multi-modal character of the posterior.

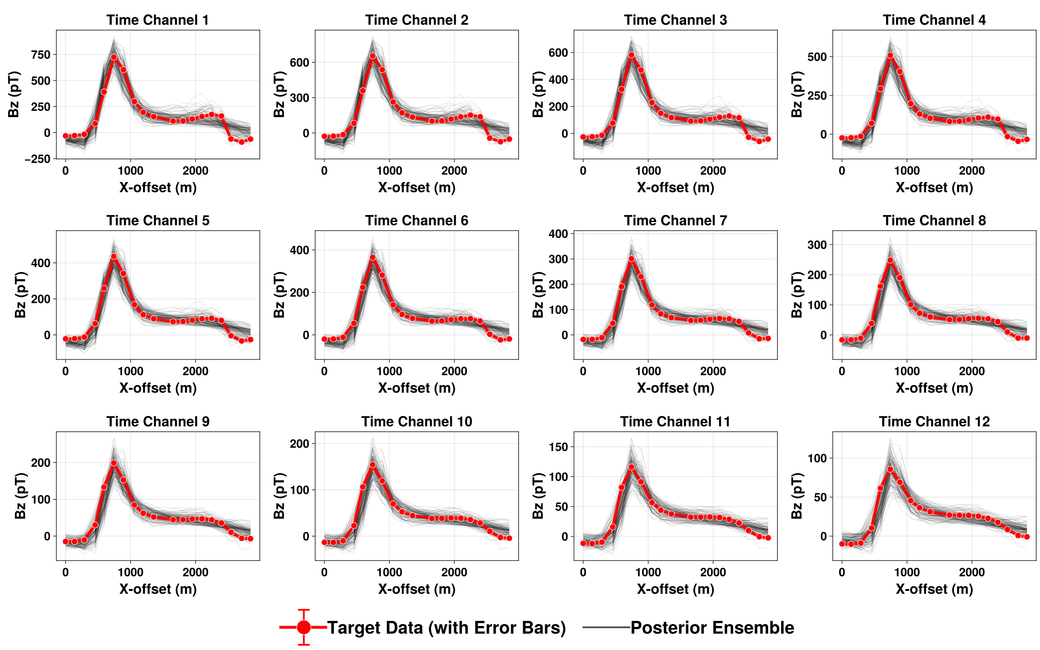

Figure 14. Ensemble of posterior EM data at each time channel for synthetic test over Gaussian true model.

Figure 15 shows the trace plots and marginal posterior distributions of the eight GP-parameters after inversion. The trace plots exhibit good mixing throughout the sampling phase, with accepted values traversing the prior range without extended periods of stagnation. The marginal posteriors show varying degrees of constraint relative to the prior. The major-axis correlation length is well-concentrated near the true value, and the log-conductivity mean and standard deviation are similarly constrained. In contrast, the marginal distributions of the bounded ZYX Euler coordinates (yaw, pitch, roll) remain relatively broad. This is consistent with the comparatively weak sensitivity of a single profile of surface EM profile to the orientation of the anisotropic covariance structure relative to its sensitivity to bulk conductivity statistics and characteristic spatial scales. Because these three coordinates jointly define a single 3D rotation, their marginal distributions should not be interpreted as independent directional distributions. Their broad support indicates that the EM data provide comparatively weak constraints on the orientation of the anisotropic covariance structure. Overall, the recovery of the dominant GP-parameters despite the unknown covariance structure demonstrates that the hierarchical Bayesian formulation can extract meaningful information about subsurface spatial statistics even in the absence of prior geological constraints.

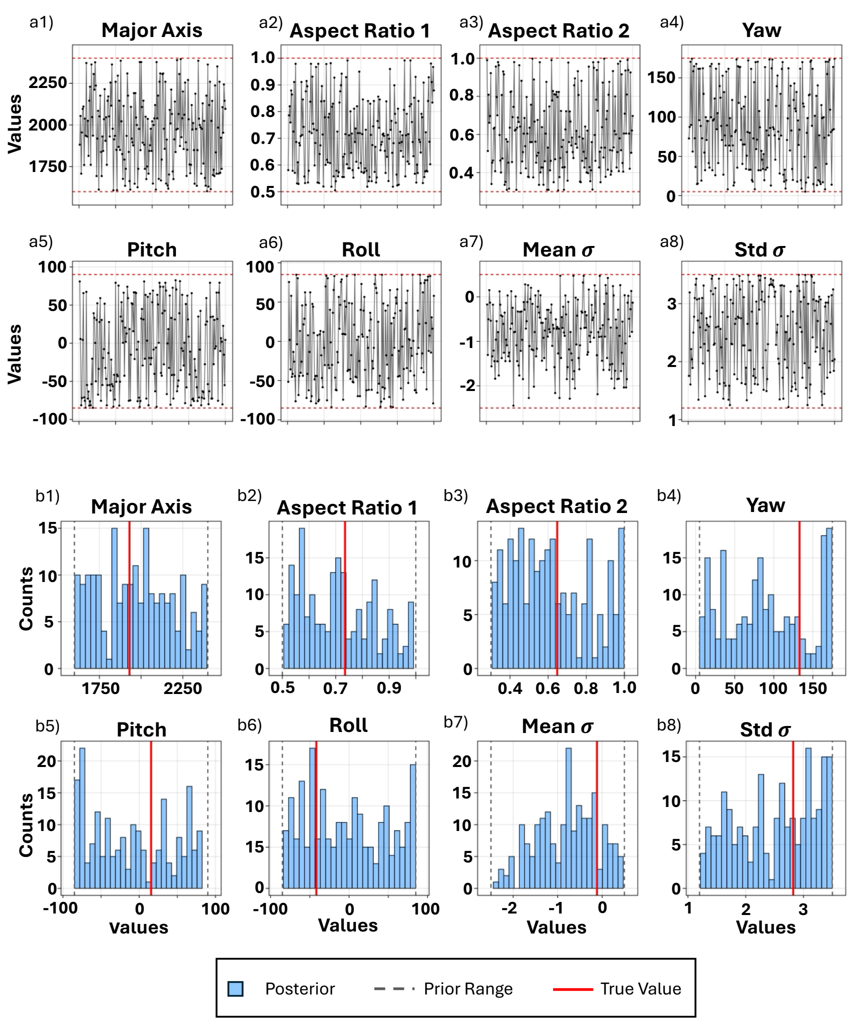

Figure 15. a) trace plot of 8 GP-parameters as chain proceeds; b) Marginal posterior distribution of GP-parameters.

To quantitatively evaluate sampling efficiency, we calculated the effective sample size (ESS) and autocorrelation length for each GP-parameter for the sampling period, as shown in Table 4. The ESS measures the number of statistically independent samples contained in each chain after accounting for serial correlation, whereas the autocorrelation length characterizes the persistence of correlation between successive samples. The retained chain contains 227–409 effective samples across the eight GP parameters, with integrated autocorrelation times of approximately 61–110 iterations, indicating moderate serial dependence but sufficient effective sampling for broad marginal characterization.

Table 4. ESS and autocorrelation length of McMC for synthetic test of covariance structure.

GP-parameter	ESS	Autocorrelation Length
$\boldsymbol{\ell_{maj}}$	339.3	73.732
$\boldsymbol{R_{mid/maj}}$	408.9	61.177
$\boldsymbol{R_{min/mid}}$	325.2	76.878
$\boldsymbol{\phi_{yaw}}$	376.1	66.541
$\boldsymbol{\phi_{pitch}}$	393.1	63.721
$\boldsymbol{\phi_{roll}}$	331.9	75.405
$\boldsymbol{\mu_{\sigma}}$	226.9	110.168
$\boldsymbol{s_{\sigma}}$	308.3	81.114

4.3. Robustness Under Prior Misspecification

To assess the robustness of the framework when the true subsurface geology violates the Gaussian prior assumption, we test two cases in which the true conductivity model is a geometrically defined discrete object rather than a GP realization. In both cases, the same surrogate and non-falsified prior used in Section 4.2 are retained without modification, so any degradation in recovery relative to Section 4.2 can be attributed directly to prior misspecification rather than surrogate error. The two cases are ordered by increasing geometric complexity: a simple ellipsoid conductor in Section 4.3.1 and a curvilinear conductor in Section 4.3.2, with the aim of characterizing how the degree of prior misspecification influences the quality and reliability of the posterior ensemble.

4.3.1. Ellipsoid Conductor

The true conductivity model in this test consists of a single ellipsoidal conductor embedded in a resistive background half-space. The conductivity values assigned to the ellipsoid and the background are both within the range of values producible by the GP prior, whereas the ellipsoid geometry presents a spatially compact but sharp-edged pattern, which represents a deliberate violation of the smooth, spatially correlated GP prior. This design provides a controlled test of robustness under prior misspecification. The surrogate and non-falsified prior from Section 4.2 are retained without modification.

The McMC chain converged successfully, with loss stabilization, temperature adaptation, and acceptance rate behave similar to those of the test over Gaussian true model in previous section. Figure 16 shows the true conductivity model, the posterior mean, and the posterior standard deviation. Despite the prior misspecification, the posterior mean recovers a clear conductivity-high in approximately the correct spatial location. The recovered anomaly is spatially diffusive relative to the true ellipsoid, lacking its sharp boundaries, which is expected because the GP prior enforces spatial smoothness on all posterior samples, so the ensemble cannot reproduce the abrupt conductivity contrast of the true model regardless of data fit. This behavior is consistent with the GP prior acting as a low-pass spatial filter, attenuating fine-scale geometric detail while preserving the broad location and amplitude of the anomaly. The posterior standard deviation is spatially structured around the recovered anomaly, with elevated variability along its margins. This indicates that the data constrain the broad presence and location of the conductivity high more strongly than its precise boundary, volume, or amplitude. The diffuse uncertainty pattern is consistent with the inability of the stationary GP prior to reproduce the sharp ellipsoidal interface exactly.

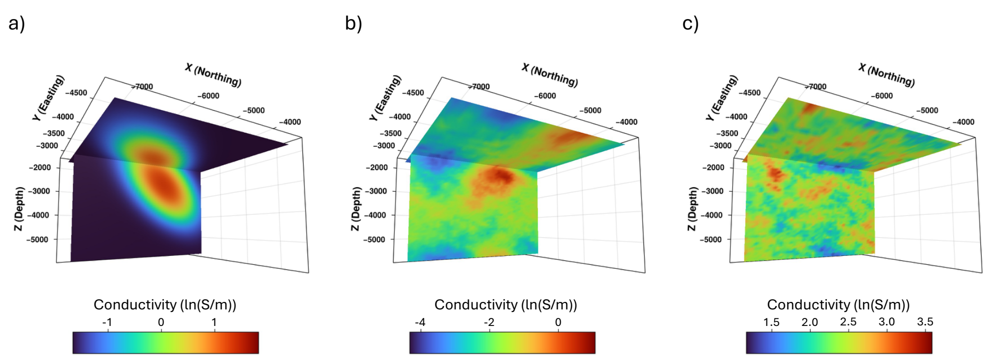

Figure 16. Posterior recovery for the synthetic test over a non-Gaussian ellipsoid conductor. a) Slices of true conductivity model; b) Slices of mean posterior conductivity model; and c) Standard deviation of posterior conductivity model. All models' values are shown in natural log scale.

Figure 17 shows the convergence of posterior data across all 12 time channels. The posterior ensemble envelops the observed signal reasonably well in early-to-mid time channels (channels 1–8), though with a wider spread than observed in the Gaussian test. Late time channels (9–12) exhibit larger ensemble spread with the predicted responses deviating more noticeably from the observations. This degradation is physically expected: late-time EM responses are sensitive to deeper and larger-scale conductivity structure, where the sharp geometric boundaries of the ellipsoid deviate most significantly from the smooth GP prior. This leads to no sufficiently compatible model being available within the GP prior family, and the posterior ensemble reflects this limitation through increased uncertainty and reduced fit quality. Nonetheless, the broad shape and amplitude of the observed signal remain captured across all channels, indicating that the framework retains meaningful data consistency even under prior misspecification.

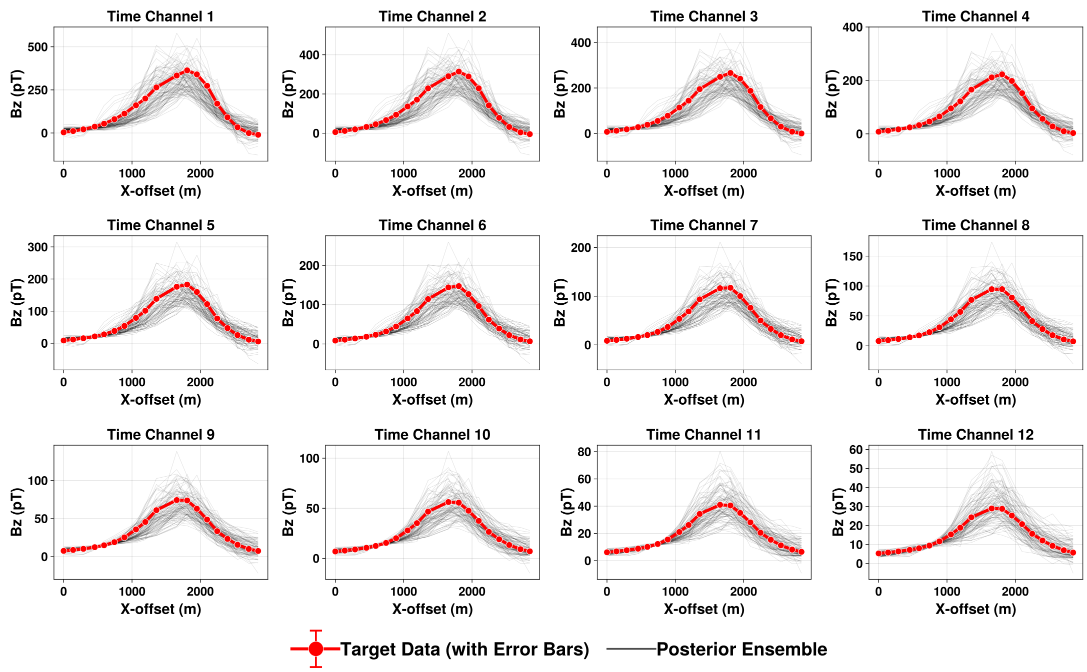

Figure 17. Ensemble of posterior EM data at each time channel for synthetic test over non-Gaussian ellipsoid true model.

To assess the reliability of the recovered conductivity-high, all accepted posterior samples are ranked by their McMC loss, and the top- and bottom-ranked models are examined alongside their predicted data fits. First row (subfigures a, b, and c) of Figure 18 shows the three accepted realizations with the lowest loss, and the second row (subfigures d, e, and f) shows the three with the highest loss. The contrast is clear that the best-fitting models all exhibit a coherent conductivity-high in the upper-left shallow region of the domain, consistent with the true ellipsoid location, against a broadly resistive background. The worst-fitting models, by contrast, show no coherent conductor in the correct location and instead display spatially chaotic conductivity patterns with no dominant anomaly. The consistent co-occurrence of a conductor in the correct location with low data loss and its absence in high-loss models confirm that the conductivity-high recovered by the posterior is a robust, data-driven feature rather than an artifact of the GP prior. This demonstrates that loss-based ranking of accepted posterior samples provides an effective and interpretable false-positive screening procedure, even when the true model violates the GP prior assumption.

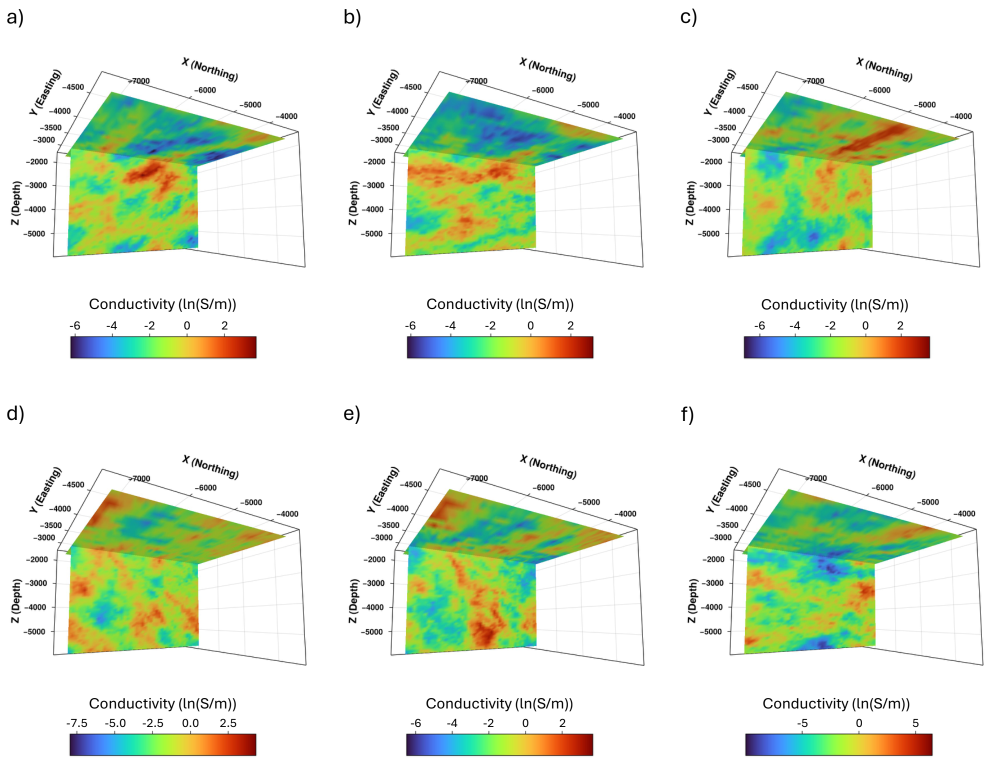

Figure 18. Loss-based false-positive screening for the ellipsoid conductor test. (a–c) The three accepted posterior realizations with the lowest McMC loss, showing a coherent conductivity-high in the correct spatial location against a resistive background. (d–f) The three accepted posterior realizations with the highest McMC loss, showing scattering conductor and spatially chaotic conductivity patterns.

4.3.2. Curvilinear Conductor

The curvilinear test represents a significantly more challenging departure from the GP prior assumption. For this test, we twist ellipsoid with sinusoidal equation shifting in vertical direction, introducing spatial curvature and directional continuity and simulating a folded structure that a stationary Gaussian covariance function cannot represent. This case is therefore not expected to yield accurate geometric recovery; rather, it serves as a boundary test to characterize the limits of the framework under extreme prior misspecification, and to assess what information, if any, can still be extracted from the data under such conditions.

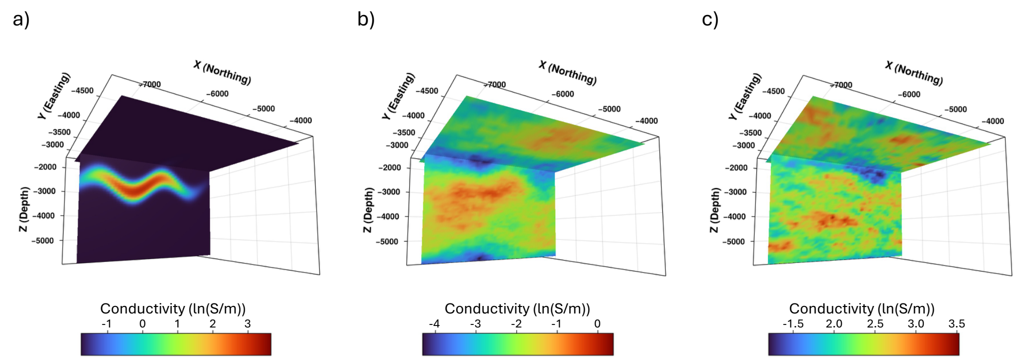

Figure 19. Posterior recovery for the synthetic test over a curvilinear conductor. a) Slices of true conductivity model; b) Slices of mean posterior conductivity model; and c) Standard deviation of posterior conductivity model. All models' values are shown in natural log scale.

Despite the geometric complexity of the true model, as shown in Figure 19, the posterior mean recovers a broadly elevated conductivity region at approximately the position of the true curvilinear conductor, though with no directional or curvilinear structure as the sinusoidal geometry is mostly smoothed out by the GP prior. Notably, the posterior standard deviation is relatively low in the region surrounding the true conductor's location and higher elsewhere in the domain, indicating that the ensemble consistently agrees on the presence of an anomaly in the correct region even though it cannot resolve its geometry. This combination of a spatially diffusive mean with locally reduced uncertainty near the true conductor reflects the low-pass filter behavior of the GP prior that the broad location and amplitude of the anomaly are captured by the ensemble, but the fine-scale geometric detail is irrecoverable within the current parameterization.

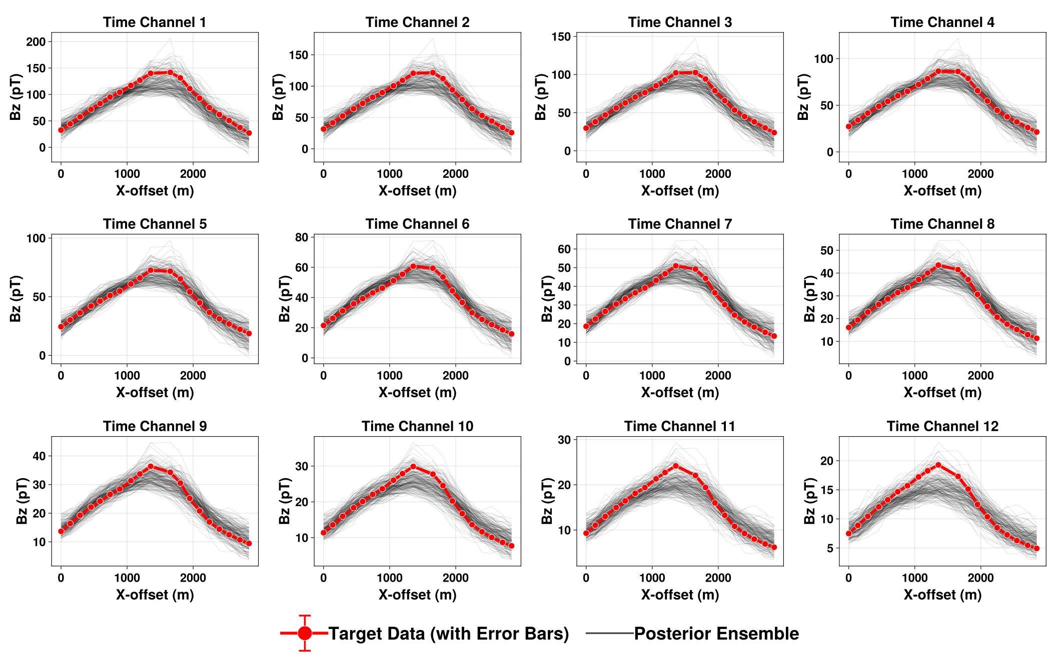

Figure 20. Ensemble of posterior EM data at each time channel for synthetic test over curvilinear true model.

The posterior data fit, shown in Figure 20, reflects this limitation. The posterior ensemble envelops the observed signal consistently and with relatively tight spread in early-to-mid time channels (1–8). However, the late time channels (9–12) tell a different story. In these time channels, the ensembles fail to envelop the observed signal, with predicted responses systematically deviating from the observations. This late-time breakdown is physically interpretable for the same reason presented in ellipsoid test of section 4.3.1, and this progressive degradation in late-time data fit quality, evolving from the Gaussian test through the ellipsoid to the curvilinear case, provides a consistent and physically interpretable picture of the framework's behavior under increasing degrees of prior misspecification.

Taken together, the ellipsoid and curvilinear tests delineate a practical boundary for the proposed framework. It is most effective when the subsurface conductivity structure is broadly consistent with a Gaussian spatial prior, either because the true geology is approximately Gaussian or because the anomaly is geometrically simple enough that its location and amplitude can be recovered even under moderate prior misspecification. For more complex geometries such as folded conductors, the GP prior acts as an increasingly severe low-pass filter, and alternative parameterizations such as multiple-point statistics or level-set methods would be required to faithfully capture the true spatial structure. Nevertheless, the ability to extract meaningful structural information from the best posterior samples even in the curvilinear case suggests that the framework retains practical diagnostic value beyond its strict prior assumptions, particularly when combined with loss-based posterior screening.

5. Field Data Application

Having validated the framework on synthetic cases of increasing complexity, we now apply it to the field TDEM dataset described in Section 2 to demonstrate its capability for 3D probabilistic inversion in a true greenfield exploration setting. The chain converges to a stable loss range of 10^{-1} to 10^{0}, roughly an order of magnitude higher than the synthetic Gaussian test, consistent with the greater structural complexity of real field data relative to a GP realization. Stage-2 proposals consistently achieve lower losses than Stage-1 throughout the chain, confirming that the delayed rejection mechanism functions as intended, and the acceptance rate stabilizes near the 0.23 target (Figure 21).

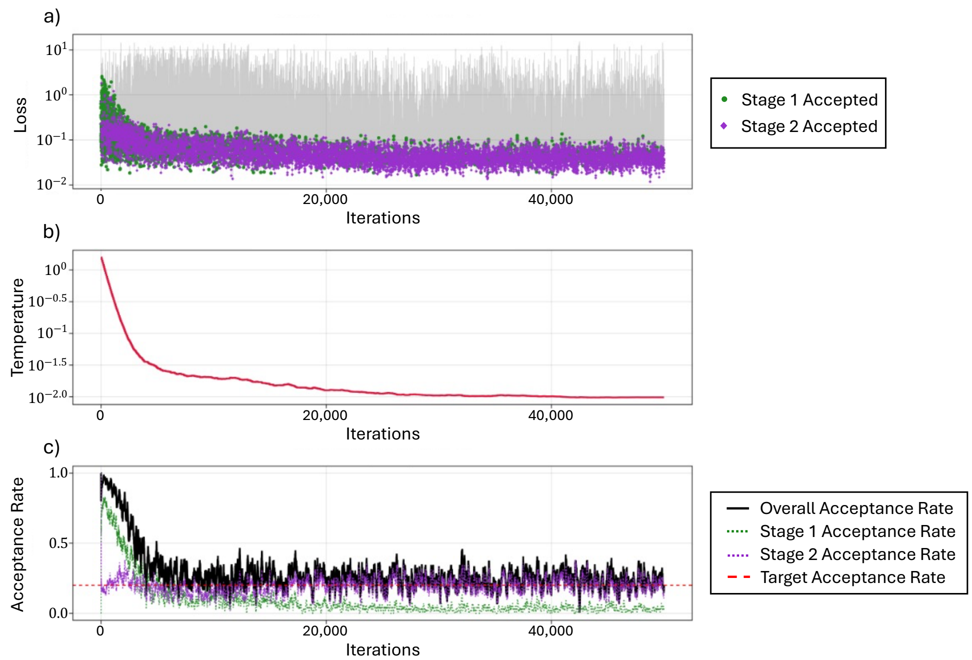

Figure 21. Convergence diagnosis plots of McMC for field test. a) Loss curve in log-10 scale, with gray dots representing all proposals, and green and purple dots indicate stage-wise acceptance; b) Temperature curve in log-10 scale; c) Moving-average acceptance rate over a sliding window of 100 iterations.

The posterior mean conductivity model reveals two spatially coherent conductivity highs consistent with the two EM anomalies identified in the field data profile (Section 2), while the posterior standard deviation is locally reduced at both anomaly locations, confirming that the ensemble consistently agrees on their presence rather than placing them by chance (Figure 22). Both features are spatially diffuse relative to what a deterministic inversion would suggest, reflecting the low-pass filtering imposed by the GP prior and the limited geometric resolution provided by a single survey profile rather than genuine ambiguity about their location. This is the same behavior characterized in the prior-misspecification tests of Section 4.2.

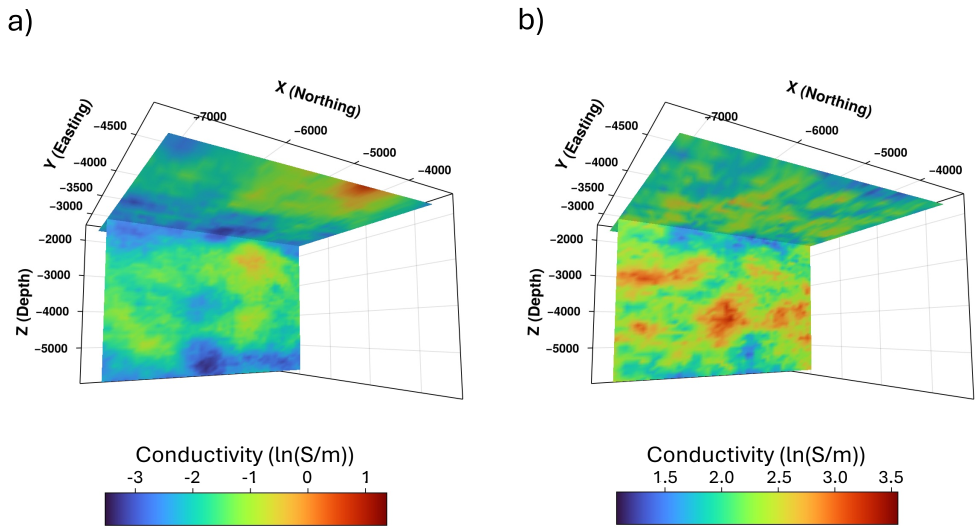

Figure 22. Posterior recovery for the field data test. a) Slices of mean posterior conductivity model; b) Standard deviation of posterior conductivity model. All models' values are shown in natural log scale.

The posterior ensemble adequately envelops the observed signal in early and intermediate channels (approximately channels 3–10), where the SNR is highest and the data carry the most reliable structural information (Figure 23). In the very earliest channels (1–2), the broader ensemble spread reflects near-surface heterogeneity at spatial scales finer than what the GP covariance function can represent, consistent with the low-pass filtering behavior documented in Section 4.2. In the latest two channels (11–12), the ensemble deviates more substantially from the observed signal. Given the low SNR at late times and the correspondingly large observational uncertainties, this is attributable to noise amplification rather than systematic model failure, and these channels contribute proportionally less to the likelihood through the noise-normalization in McMC loss (Equation 22). The intermediate channels therefore constitute the primary data constraint, and the posterior ensemble demonstrates adequate data consistency within this informative window.

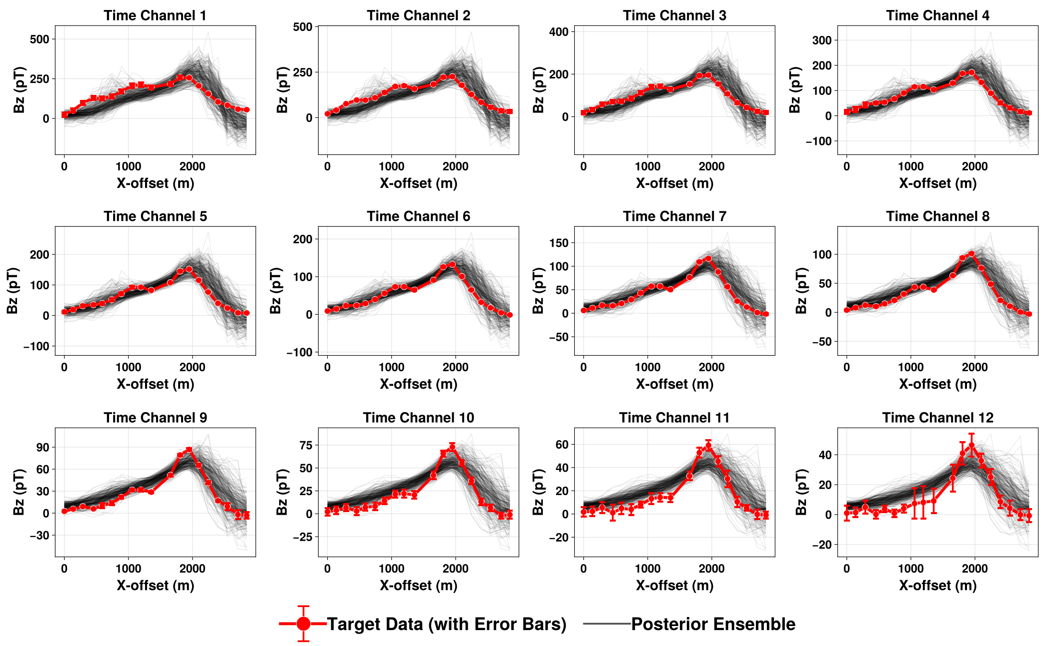

Figure 23. Ensemble of posterior EM data at each time channel for field data test.

The distribution of posterior GP-parameters in Figure 24 shows that the log-conductivity mean and standard deviation have clear posterior contraction relative to the prior, consistent with the sensitivity analysis finding that these two parameters most strongly control the EM response amplitude and decay shape. In contrast, the major-axis correlation length and aspect ratios retain a broad and multimodal posterior across the prior range, indicating that the single survey profile provides limited geometric constraint on the dominant spatial scale of the conductor. The data are consistent with multiple spatial regimes that a multi-line 3D inversion would be needed to discriminate. The orientation angles similarly retain broad posteriors spanning a substantial fraction of the prior range, which is expected given that a single profile samples only one cross-section through a 3D body and carries little sensitivity to out-of-plane geometry. Taken together, the posterior GP-parameters correctly reflect what the data can and cannot resolve: bulk conductivity statistics are well-constrained, while spatial geometry remains ambiguous without additional survey coverage.

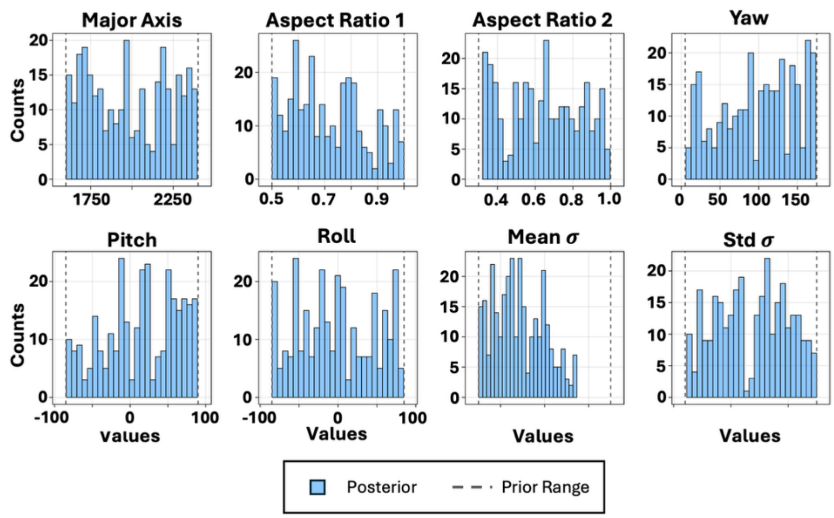

Figure 24. Marginal posterior distribution of 8 GP-parameters.

To assess the robustness of the recovered conductivity anomalies, all accepted posterior samples are ranked by their McMC loss, and the three lowest- and highest-loss realizations are examined in Figure 25. The best-fitting models (a–c) consistently reproduce a coherent conductivity high in the right-side anomaly location against a broadly resistive background. This pattern coincides with the persisting high-value section to the right side of the data profile, confirming that this feature is data-driven rather than an artifact of the GP prior. The left-side anomaly, by contrast, does not appear consistently in the best-fitting realizations, suggesting that its signature in the informative intermediate channels could be insufficiently distinct to be reliably resolved within the current GP parameterization and single-profile survey geometry. The worst-fitting models (d–f) show spatially chaotic conductivity patterns with no coherent anomaly at either location, a contrast that directly parallels the false-positive screening results of the synthetic ellipsoid test (Section 4.3.1). Taken together, the loss-based ranking identifies the right-side conductor as a robust, data-driven target, while appropriately flagging the left-side anomaly as uncertain.

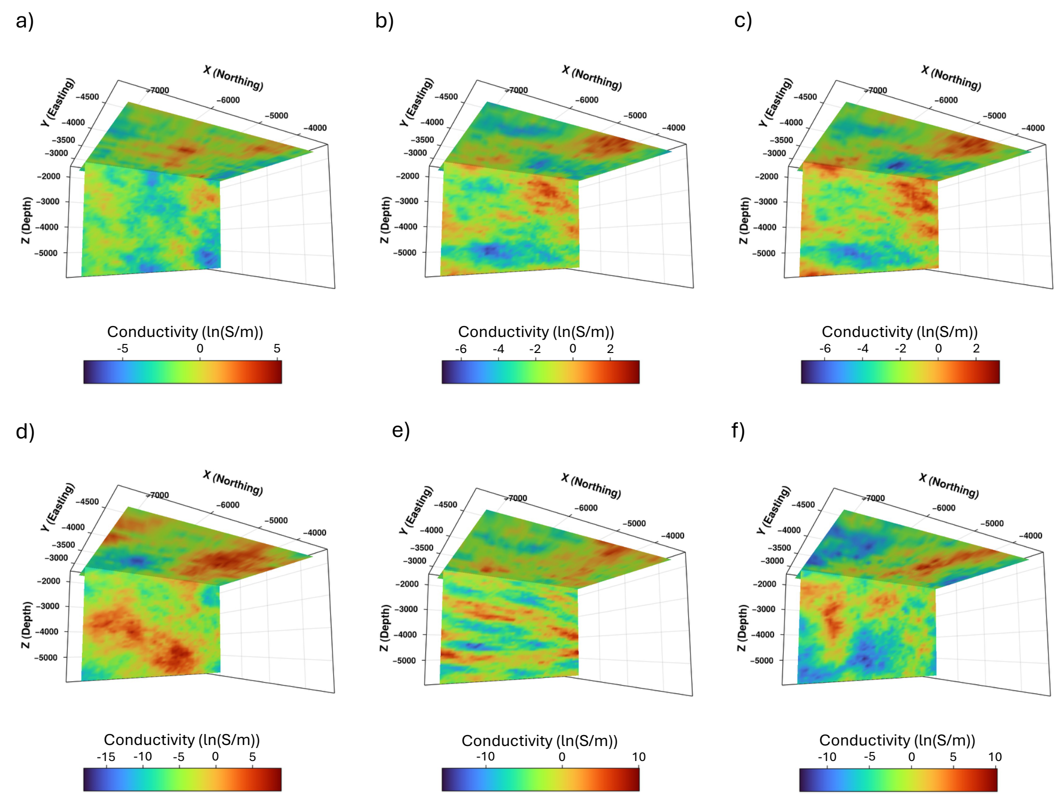

Figure 25. Loss-based false-positive screening for the field test. (a–c) The three accepted posterior realizations with the lowest McMC loss, showing a coherent conductivity-high to the right shallow area, which coincides with persisting high-response section in data profile (d–f) The three accepted posterior realizations with the highest McMC loss, showing scattering conductor and spatially chaotic conductivity patterns.

5.1.Posterior Validation against PDE-based Forward Modeling

While the surrogate validation in Section 3.3.1 establishes that the network generalizes accurately within the non-falsified prior range, it remains important to verify that accepted posterior samples that are concentrated in a subregion of that prior range determined by the field data are also reproduced faithfully by the true PDE-based forward solver. To provide an illustrative check, we randomly picked one accepted posterior realization, and its surrogate-predicted responses are compared directly against full SimPEG forward simulations across all 12 selected time channels, as shown in Figure 26.

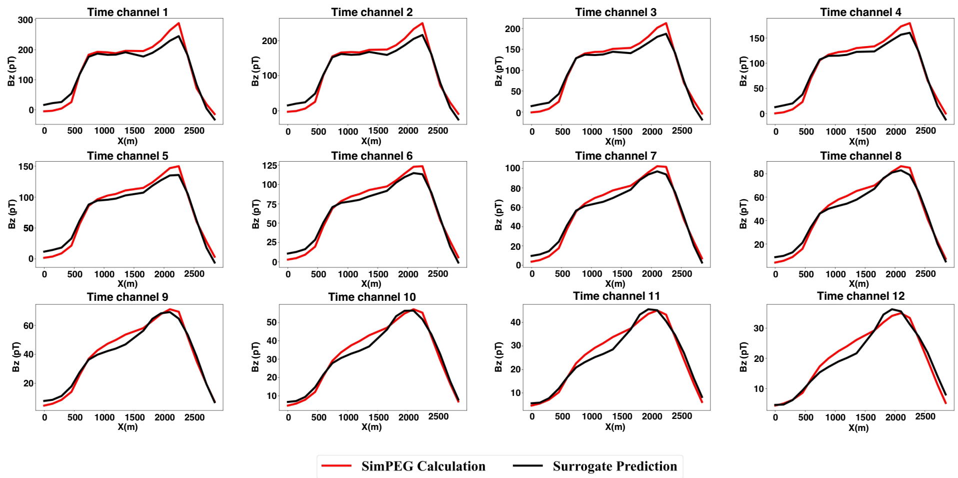

Figure 26. Comparison between surrogate-predicted and PDE-based EM data sets from one of posterior conductivity-model realizations.

The surrogate predictions closely track the SimPEG-calculated responses in both amplitude and spatial pattern across all channels, with discrepancies remaining small throughout the early-to-intermediate time channels where the signal-to-noise ratio is highest and the data carry the most structural information. Some deviation is visible at later time channels, consistent with the reduced dynamic range and lower surrogate accuracy at those gates documented in Section 3.3.1.

It is worth noting that in a stochastic inversion framework, perfect surrogate-PDE agreement on any individual posterior sample, although desired, is not a strict requirement. Unlike deterministic inversion where the accuracy of a single optimal model is paramount, the inference here relies on the statistical properties of a converged posterior ensemble of tens of thousands of samples. Small per-sample surrogate approximation errors are therefore partially averaged out across the ensemble, and the posterior mean and uncertainty estimates are more robust to individual surrogate inaccuracies than any single realization would suggest. What matters is that the surrogate is sufficiently accurate to guide the McMC chain toward the correct posterior region, which is a condition supported by the data fitting results and the loss-based screening. The comparison in Figure 26 supports that this condition is met for the field posterior, and we regard the observed level of surrogate-PDE agreement as adequate for the purposes of probabilistic inference in this setting.

6. Discussion

Several observations from both the synthetic and field results merit further discussion, as they reveal both the capabilities and the boundaries of the proposed framework in a way that is instructive for future applications.

The sensitivity analysis in Section 3.2.1 already established that the major-axis correlation length, aspect ratios, and orientation angles are relatively insensitive parameters given the field dataset, and the posterior GP-parameter distributions in Section 5 confirm this. The geometry-controlling parameters retain broad, multimodal posteriors while bulk conductivity statistics contract meaningfully. This is not a failure of the sampler but a faithful reflection of what a single survey profile can resolve. A ground TDEM profile samples the subsurface along one cross-section, and the recorded transient responses integrate contributions from a 3D volume. The data therefore constrain the bulk electrical character of that volume more reliably than its internal geometry. Extending the inversion to multiple profiles would introduce cross-line spatial constraints that could substantially reduce this geometric ambiguity, and we regard multi-line 3D inversion as the natural next step for this framework.

From an algorithmic perspective, the PPM construction is conceptually related to function-space samplers such as the preconditioned Crank–Nicolson (pCN) method, in that both construct proposals that preserve a reference prior measure. The pCN is formulated directly for Gaussian reference measures and is designed to avoid the deterioration in sampling efficiency that conventional random-walk proposals experience under mesh refinement (Cotter et al., 2013). In contrast, PPM operates component-wise in an underlying uniform probability space, which allows the latent Gaussian field and bounded GP hyperparameters to be treated within a common proposal framework and assigned separate group-level perturbation strengths. This flexibility is useful for the present hierarchical formulation, where both the field realization and covariance parameters are unknown. However, mesh-independent convergence of the present PPM implementation has not been established, and a direct comparison with pCN remains an important subject for future investigation.

A subtler but important observation concerns the behavior of the posterior mean across different synthetic test cases. In the Gaussian true model test, the posterior mean appears smooth and largely featureless, offering little direct hint of the true conductivity structure. In the ellipsoid test, by contrast, the posterior mean clearly localizes a conductivity high at approximately the correct position. These two outcomes are not contradictory, but a picturesque example of non-uniqueness problem that has persisted for a decades in geophysical data interpretation. Understanding why they differ is instructive for how the mean model should be interpreted in practice. When the true model is a Gaussian field, conductivity highs and lows are spatially distributed across the entire domain, and different posterior realizations recover different subsets of these features in different locations. Their ensemble average cancels the local variability, producing a smooth mean that reflects no single feature but is consistent with all of them. When the true model is a spatially compact ellipsoid, nearly every data-consistent realization must place a conductivity anomaly in approximately the same location to reproduce the localized EM signal. In such a case, the averaging reinforces rather than cancels the anomaly. This distinction reveals a general principle that the posterior mean is most informative when the anomaly is spatially confined and the signal is dominated by a single source region, and least informative when the subsurface is heterogeneous and the signal integrates contributions from many distributed features. Notably, the posterior mean in the heterogeneous case closely approximates what a deterministic inversion would produce: a smooth, featureless model that fits the data but conceals the true complexity of the subsurface. This is not a coincidence. Deterministic inversion with smoothness regularization and a single optimal model is effectively computing a weighted mean over plausible models, and our results show precisely what that averaging operation destroys. In the ellipsoid case, where the signal is dominated by a single compact source, the mean recovers the anomaly, and deterministic inversion would likely do the same. In the Gaussian heterogeneous case, the mean washes out all structure, and a geologist relying on it alone would significantly underestimate the complexity and non-uniqueness of the subsurface. The posterior ensemble, particularly the spread and diversity across individual realizations, is therefore not a refinement of the deterministic result but a fundamentally different and more complete characterization of the inverse problem.

The data fitting quality of the field data test is less precise than the synthetic Gaussian test, with a higher loss floor and broader data fit envelopes in the intermediate channels. This is expected. Real geology is under no obligation to conform to a rigorous stationary Gaussian prior, and the Midcontinent Rift setting almost certainly contains structural complexity, including sharp lithological boundaries, fault contacts, and folded stratigraphy, that the GP parameterization cannot represent. The GP prior acts as a low-pass spatial filter, and while this is sufficient to recover the bulk location and amplitude of a conductor, it will systematically underfit any sharp-edged or curvilinear feature, as the synthetic prior-misspecification tests demonstrate. Extending the parameterization to accommodate more complex geological structures, for example through multiple-point statistics priors or level-set representations, would improve geometric fidelity, though at the cost of significantly greater complexity in the surrogate training and MCMC proposal design. We regard this as an important direction for future work, particularly in structurally complex terrains where Gaussian continuity is a poor approximation.

A related limitation concerns the surrogate architecture. The U-Net used in this work is well-suited to capturing the spatial encoding and decoding of 3D conductivity fields, but its convolutional structure is not specifically designed to represent the diffusive physics of transient EM wave propagation. The temporal decay of the EM signal is governed by a diffusion equation, and architectures with explicit temporal memory, such as long short-term memory networks (LSTMs) or transformer-based sequence models, may better approximate the channel-to-channel dependencies in the multi-time-channel response. We have not tested alternative architectures in this work, but the surrogate is a modular component of the framework and could in principle be replaced without modifying the McMC or PPM components. Investigating architectures that more explicitly encode the physics of EM diffusion remains an open and promising research direction.

A fundamental concern in any surrogate-accelerated inversion is distribution shift, that the surrogate is trained on prior samples and may be inaccurate for models that the McMC chain visits during posterior sampling, particularly if the posterior occupies a region of model space that is underrepresented in the training ensemble. Prior falsification mitigates this by ensuring the training ensemble covers the data-consistent region of model space before inversion begins. The in-distribution surrogate validation in Section 3.3.1 confirms that the network achieves a mean NMSE of 0.83% on held-out prior samples, and the direct comparison against full SimPEG simulations for accepted posterior sample in Section 5.1 further supports that the surrogate operates as an accurate proxy within the dominant posterior modes of the field inversion. Nevertheless, prior falsification cannot fully eliminate distribution shift if the posterior concentrates in a region of model space that was only sparsely represented in the surrogate-training ensemble. The remaining discrepancy between the surrogate and PDE-based responses may therefore partly reflect this residual limitation in training-set coverage. One potential remedy is surrogate fine-tuning during the McMC chain itself: accepted posterior samples could be used to augment the training set and periodically retrain the surrogate, progressively improving its accuracy in the posterior region. However, the computational cost of this approach is non-trivial, and the retraining target shifts continuously as the chain evolves, which ultimately compromises tractability. We propose this as a concrete direction for improving surrogate fidelity in future implementations. More broadly, it is worth emphasizing that the stochastic nature of the inference provides an inherent degree of robustness to per-sample surrogate approximation errors: since the posterior is characterized by a converged ensemble of tens of thousands of samples rather than any single model, small individual inaccuracies are partially averaged out across realizations, and the ensemble-level statistics are more resilient to surrogate imperfection than a deterministic inversion result would be. This distinction is a structural advantage of surrogate-accelerated McMC over surrogate-accelerated deterministic optimization, where a single biased forward evaluation could corrupt the final result entirely.

Finally, while this work focuses on ground-loop TDEM data, the framework is broadly transferable to other geophysical survey types, and it enables capabilities beyond what was demonstrated here in some configurations. For airborne EM systems, the simpler and geometrically consistent transmitter-receiver configuration makes 2D inversion along individual flight lines natural, and the corresponding surrogate would be faster to evaluate and easier to train than the 3D surrogate model used in this work. This opens the possibility of near-real-time probabilistic inversion: data collected on the current flight line could be processed and inverted while the aircraft surveys the next line, delivering uncertainty-quantified subsurface models continuously during acquisition rather than weeks afterward. The same principle extends to potential field methods, including gravity and magnetic surveys, where the forward operators are linear and computationally inexpensive, making even full 3D probabilistic inversion with real-time turnaround conceivable. As geophysical acquisition rates continue to increase and critical mineral exploration expands to cover larger and more remote areas, the ability to deliver uncertainty-aware subsurface models at acquisition speed represents a practically significant advance over the current norm of post-survey deterministic inversion.

7. Conclusion

This work demonstrates that rigorous 3D probabilistic inversion of TDEM data is computationally achievable in greenfield exploration settings by combining GP parameterization with unknown covariance, a U-Net surrogate forward model, and a PPM-based McMC sampler with delayed rejection and adaptive annealing. The surrogate reduces the per-iteration forward cost by a factor of approximately 10^4, making 50,000-iteration 3D McMC chains tractable on a single workstation. The synthetic validation establishes that the framework correctly characterizes the posterior when the prior is well-specified and recovers the broad location and amplitude of anomalies even under prior misspecification. Loss-based false-positive screening consistently distinguishes data-driven conductivity features from prior artifacts across all test cases. The field application further confirms that the posterior mean approximates what a deterministic inversion would produce, while the diversity across individual realizations reveals the non-uniqueness that smoothness-regularized deterministic approaches conceal. The primary conductor anomaly in the field dataset is identified as a more robustly supported and higher-priority anomaly, while the secondary anomaly is flagged as uncertain under the current single-profile survey geometry. Future priorities include multi-line inversion to resolve geometric ambiguity, surrogate architectures that more explicitly encode EM diffusion physics, and extension to airborne EM and potential field methods where simpler forward operators open the possibility of near-real-time probabilistic inversion during data acquisition.

8. Acknowledgements

We thank members of the Mineral-X industrial affiliates program for funding this work.

9. Data and code availability

Field data used in this work is available upon reasonable request to correspondence author. Code is available at https://github.com/Stanford-Mineral-X/EM_Surrogate_Inv3D.

10. Statement and Declarations

Conflict of Interests: the authors declare that they have no known competing financial interests or personal relationships that could have appeared to influence the work reported in this paper.

References

Aghasi, Alireza, Misha Kilmer, and Eric L. Miller. "Parametric level set methods for inverse problems." SIAM Journal on Imaging Sciences 4, no. 2 (2011): 618-650.

Ardizzone, Lynton, Jakob Kruse, Sebastian Wirkert, Daniel Rahner, Eric W. Pellegrini, Ralf S. Klessen, Lena Maier-Hein, Carsten Rother, and Ullrich Köthe. "Analyzing inverse problems with invertible neural networks." arXiv preprint arXiv:1808.04730 (2018).

Auken, Esben, Anders Vest Christiansen, Casper Kirkegaard, Gianluca Fiandaca, Cyril Schamper, Ahmad Ali Behroozmand, Andrew Binley et al. "An overview of a highly versatile forward and stable inverse algorithm for airborne, ground-based and borehole electromagnetic and electric data." Exploration Geophysics 46, no. 3 (2015): 223-235.

Barnes, Stephen J., Alexander R. Cruden, Nicholas Arndt, and Benoit M. Saumur. "The mineral system approach applied to magmatic Ni–Cu–PGE sulphide deposits." Ore geology reviews 76 (2016): 296-316.

Bittar, George, Sihong Wu, Yawei Su, Shubin Zeng, Jiajia Sun, Xuqing Wu, Yueqin Huang, and Jiefu Chen. "Invertible neural network for real-time inversion and uncertainty quantification of ultra-deep resistivity measurements." Computers & Geosciences (2025): 106067.

Börner, Ralph-Uwe, Oliver G. Ernst, and Stefan Güttel. "Three-dimensional transient electromagnetic modelling using rational Krylov methods." Geophysical Journal International 202, no. 3 (2015): 2025-2043.

Bui-Thanh, Tan, Omar Ghattas, James Martin, and Georg Stadler. 2013. “A Computational Framework for Infinite-Dimensional Bayesian Inverse Problems Part I: The Linearized Case, with Application to Global Seismic Inversion.” SIAM Journal on Scientific Computing 35 (6): A2494–A2523. https://doi.org/10.1137/12089586X.

Caers, Jef, and Todd Hoffman. "The probability perturbation method: A new look at Bayesian inverse modeling." Mathematical geology 38, no. 1 (2006): 81-100.

Caers, Jef Karel, Peng Li, Jonas Kloeckner, Juan Pablo Daza, David Zhen Yin, and Céline Scheidt. 2026. "Stochastic Inversion of Geophysical Data by Sequential Bayesian Updating Under a Non-Stationary Gaussian Process Prior" Minerals 16, no. 7: 736. https://doi.org/10.3390/min16070736 Caers, Jef. "History matching under training-image-based geological model constraints." SPE journal 8, no. 03 (2003): 218-226.

Cannon, William F. "The Midcontinent rift in the Lake Superior region with emphasis on its geodynamic evolution." Tectonophysics 213, no. 1-2 (1992): 41-48.

Chan, Shing, and Ahmed H. Elsheikh. "Parametrization and generation of geological models with generative adversarial networks." arXiv preprint arXiv:1708.01810 (2017).

Christensen, Nikolaj Kruse, Burke J. Minsley, and Steen Christensen. "Generation of 3-D hydrostratigraphic zones from dense airborne electromagnetic data to assess groundwater model prediction error." Water Resources Research 53, no. 2 (2017): 1019-1038.

Cockett, Rowan, Seogi Kang, Lindsey J. Heagy, Adam Pidlisecky, and Douglas W. Oldenburg. "SimPEG: An open source framework for simulation and gradient based parameter estimation in geophysical applications." Computers & Geosciences 85 (2015): 142-154.

Dietrich, Colin R., and Garry N. Newsam. "A fast and exact method for multidimensional Gaussian stochastic simulations." Water Resources Research 29, no. 8 (1993): 2861-2869.

Engebretsen, Kim Wann, Bo Zhang, Gianluca Fiandaca, Line Meldgaard Madsen, Esben Auken, and Anders Vest Christiansen. "Accelerated 2.5-D inversion of airborne transient electromagnetic data using reduced 3-D meshing." Geophysical Journal International 230, no. 1 (2022): 643-653.

Fenwick, Darryl, Céline Scheidt, and Jef Caers. "Quantifying asymmetric parameter interactions in sensitivity analysis: application to reservoir modeling." Mathematical Geosciences 46, no. 4 (2014): 493-511.

Gelfand, Alan E., and Adrian FM Smith. "Sampling-based approaches to calculating marginal densities." Journal of the American statistical association 85, no. 410 (1990): 398-409.

Gelman, Andrew, Walter R. Gilks, and Gareth O. Roberts. "Weak convergence and optimal scaling of random walk Metropolis algorithms." The annals of applied probability 7, no. 1 (1997): 110-120.

Giraud, Jérémie, Mark Lindsay, and Mark Jessell. "Generalization of level-set inversion to an arbitrary number of geologic units in a regularized least-squares framework." Geophysics 86, no. 4 (2021): R623-R637.

Green, Peter J., and Antonietta Mira. "Delayed rejection in reversible jump Metropolis–Hastings." Biometrika 88, no. 4 (2001): 1035-1053.

Haber, Eldad, Uri M. Ascher, and Doug Oldenburg. "On optimization techniques for solving nonlinear inverse problems." Inverse problems 16, no. 5 (2000): 1263-1280.

Hansen, Thomas Mejer, Knud Skou Cordua, Bo Holm Jacobsen, and Klaus Mosegaard. "Accounting for imperfect forward modeling in geophysical inverse problems—exemplified for crosshole tomography." Geophysics 79, no. 3 (2014): H1-H21.

Hastings, W. Keith. "Monte Carlo sampling methods using Markov chains and their applications." (1970): 97-109.

Kingma, Diederik P., and Jimmy Ba. "Adam: A method for stochastic optimization." arXiv preprint arXiv:1412.6980 (2014).

Kirkpatrick, Scott, C. Daniel Gelatt Jr, and Mario P. Vecchi. "Optimization by simulated annealing." science 220, no. 4598 (1983): 671-680.

Kitanidis, Peter K. "On the geostatistical approach to the inverse problem." Advances in Water Resources 19, no. 6 (1996): 333-342.

Kitanidis, Peter K. "Parameter uncertainty in estimation of spatial functions: Bayesian analysis." Water resources research 22, no. 4 (1986): 499-507.

Kitanidis, Peter K. 1995. “Quasi-Linear Geostatistical Theory for Inversing.” Water Resources Research 31 (10): 2411–2419. doi:10.1029/95WR01945.

Knight, Rosemary, Ryan Smith, Ted Asch, Jared Abraham, Jim Cannia, Andrea Viezzoli, and Graham Fogg. "Mapping aquifer systems with airborne electromagnetics in the Central Valley of California." Groundwater 56, no. 6 (2018): 893-908.

Kwan, Karl, and Stephen Reford. "Innovative airborne geophysical strategies to assist the exploration of critical metal systems." Geosystems and Geoenvironment 4, no. 1 (2025): 100344.

Laloy, Eric, Romain Hérault, Diederik Jacques, and Niklas Linde. "Training‐image based geostatistical inversion using a spatial generative adversarial neural network." Water Resources Research 54, no. 1 (2018): 381-406.

Lightfoot, Peter C., and Dawn Evans-Lamswood. "Structural controls on the primary distribution of mafic–ultramafic intrusions containing Ni–Cu–Co–(PGE) sulfide mineralization in the roots of large igneous provinces." Ore Geology Reviews 64 (2015): 354-386.

Linde, Niklas, Philippe Renard, Tapan Mukerji, and Jef Caers. "Geological realism in hydrogeological and geophysical inverse modeling: A review." Advances in Water Resources 86 (2015): 86-101.

Liu, Mingliang, Dario Grana, Klaus Mosegaard, Mrinal K. Sen, Minghui Xu, and Tapan Mukerji. "Bayesian inference for subsurface geophysical inverse problems." Reviews of Geophysics 64, no. 1 (2026): e2025RG000884.

Liu, Yunhe, Zhiyuan Ke, Changchun Yin, Changkai Qiu, Zhihao Rong, Xinpeng Ma, Xu Yang et al. "Efficient uncertainty quantification for three-dimensional MT inversion via variational inference." IEEE Transactions on Geoscience and Remote Sensing (2025).

Lopez‐Alvis, Jorge, Frederic Nguyen, M. C. Looms, and Thomas Hermans. "Geophysical inversion using a variational autoencoder to model an assembled spatial prior uncertainty." Journal of Geophysical Research: Solid Earth 127, no. 3 (2022): e2021JB022581.

Mariethoz, Gregoire, and Jef Caers. Multiple-point geostatistics: stochastic modeling with training images. John Wiley & Sons, 2015.

McKay, Michael D., Richard J. Beckman, and William J. Conover. "A comparison of three methods for selecting values of input variables in the analysis of output from a computer code." Technometrics 42, no. 1 (2000): 55-61.

McMillan, Michael S., Christoph Schwarzbach, Eldad Haber, and Douglas W. Oldenburg. "3D parametric hybrid inversion of time-domain airborne electromagnetic data." Geophysics 80, no. 6 (2015): K25-K36.

Metropolis, Nicholas, Arianna W. Rosenbluth, Marshall N. Rosenbluth, Augusta H. Teller, and Edward Teller. "Equation of state calculations by fast computing machines." The journal of chemical physics 21, no. 6 (1953): 1087-1092.

Mo, Shaoxing, Nicholas Zabaras, Xiaoqing Shi, and Jichun Wu. "Integration of adversarial autoencoders with residual dense convolutional networks for estimation of non‐Gaussian hydraulic conductivities." Water Resources Research 56, no. 2 (2020): e2019WR026082.

Moghadas, Davood, Ahmad A. Behroozmand, and Anders Vest Christiansen. 2020. "Soil Electrical Conductivity Imaging Using a Neural Network-Based Forward Solver: Applied to Large-Scale Bayesian Electromagnetic Inversion." Journal of Applied Geophysics 176: 104012. doi:10.1016/j.jappgeo.2020.104012.

Mosegaard, Klaus, and Albert Tarantola. "Monte Carlo sampling of solutions to inverse problems." Journal of Geophysical Research: Solid Earth 100, no. B7 (1995): 12431-12447.

Mosser, Lukas, Olivier Dubrule, and Martin J. Blunt. "Stochastic seismic waveform inversion using generative adversarial networks as a geological prior." Mathematical Geosciences 52, no. 1 (2020): 53-79.

Nabighian, Misac N. "Quasi-static transient response of a conducting half-space—An approximate representation." Geophysics 44, no. 10 (1979): 1700-1705.

Nabighian, Misac N., and James C. Macnae. "Time domain electromagnetic prospecting methods." (1991).

Oldenburg, Douglas W., and Yaoguo Li. "Inversion for applied geophysics: A tutorial." (2005).

Polette, Nadège, Olivier Le Maître, Pierre Sochala, and Alexandrine Gesret. "Change of measure for Bayesian field inversion with hierarchical hyperparameters sampling." Journal of Computational Physics 529 (2025): 113888.

Puzyrev, Vladimir, and Andrei Swidinsky. "Inversion of 1D frequency-and time-domain electromagnetic data with convolutional neural networks." Computers & geosciences 149 (2021): 104681.

Robbins, Herbert, and Sutton Monro. "A stochastic approximation method." The annals of mathematical statistics (1951): 400-407.

Rodriguez, Oscar, Jamie M. Taylor, and David Pardo. "Multimodal variational autoencoder for inverse problems in geophysics: Application to a 1-D magnetotelluric problem." Geophysical Journal International 235, no. 3 (2023): 2598-2613.

Ronneberger, Olaf, Philipp Fischer, and Thomas Brox. "U-net: Convolutional networks for biomedical image segmentation." In International Conference on Medical image computing and computer-assisted intervention, pp. 234-241. Cham: Springer international publishing, 2015.

Sambridge, Malcolm, and Klaus Mosegaard. "Monte Carlo methods in geophysical inverse problems." Reviews of Geophysics 40, no. 3 (2002): 3-1.

Spies, Brian R. "Depth of investigation in electromagnetic sounding methods." Geophysics 54, no. 7 (1989): 872-888.

Strebelle, Sebastien. "Conditional simulation of complex geological structures using multiple-point statistics." Mathematical geology 34, no. 1 (2002): 1-21.

Stuart, Andrew M. 2010. “Inverse Problems: A Bayesian Perspective.” Acta Numerica 19: 451–559. https://doi.org/10.1017/S0962492910000061.

Tarantola, Albert, and Bernard Valette. "Generalized nonlinear inverse problems solved using the least squares criterion." Reviews of Geophysics 20, no. 2 (1982): 219-232.

Tarantola, Albert. Inverse problem theory and methods for model parameter estimation. Society for industrial and applied mathematics, 2005.

Tierney, Luke, and Antonietta Mira. "Some adaptive Monte Carlo methods for Bayesian inference." Statistics in medicine 18, no. 17‐18 (1999): 2507-2515.

Tikhonov, Andrei Nikolaevich. "On the regularization of ill-posed problems." In Doklady Akademii Nauk, vol. 153, no. 1, pp. 49-52. Russian Academy of Sciences, 1963.

Walker, Matthew, and Andrew Curtis. "Spatial Bayesian inversion with localized likelihoods: an exact sampling alternative to McMC." Journal of Geophysical Research: Solid Earth 119, no. 7 (2014): 5741-5761.

Wang, Lijing, Peter K. Kitanidis, and Jef Caers. "Hierarchical bayesian inversion of global variables and large‐scale spatial fields." Water Resources Research 58, no. 5 (2022): e2021WR031610.

Wu, Sihong, Qinghua Huang, and Li Zhao. "A deep learning-based network for the simulation of airborne electromagnetic responses." Geophysical Journal International 233, no. 1 (2023): 253-263.

Wu, Sihong, Qinghua Huang, and Li Zhao. "Fast Bayesian inversion of airborne electromagnetic data based on the invertible neural network." IEEE Transactions on Geoscience and Remote Sensing 61 (2023): 1-11.

Xiao, Sinan, Teng Xu, Sebastian Reuschen, Wolfgang Nowak, and Harrie‐Jan Hendricks Franssen. "Bayesian Inversion of Multi‐Gaussian Log‐Conductivity Fields With Uncertain Hyperparameters: An Extension of Preconditioned Crank‐Nicolson Markov Chain Monte Carlo With Parallel Tempering." Water resources research 57, no. 9 (2021): e2021WR030313.

Yang, Dikun, and Douglas W. Oldenburg. "Three-dimensional inversion of airborne time-domain electromagnetic data with applications to a porphyry deposit." Geophysics 77, no. 2 (2012): B23-B34.

Yang, Xu, Yunhe Liu, Yang Su, Changchun Yin, Luyuan Wang, Yu Gao, Xiuyan Ren, and Bo Zhang. "An efficient Bayesian inference for geo-electromagnetic data inversion based on surrogate modeling with adaptive sampling DNN." IEEE Transactions on Geoscience and Remote Sensing 62 (2024): 1-17.

Yin, Zhen, Alex Miltenberger, Mark Topinka, Lijing Wang, Tapan Mukerji, and Jef Caers. "Quantifying model misrepresentation in geophysical inversion for critical mineral exploration." IEEE Transactions on Geoscience and Remote Sensing (2025).

Zheglova, P., C. G. Farquharson, and C. A. Hurich. "2-D reconstruction of boundaries with level set inversion of traveltimes." Geophysical Journal International 192, no. 2 (2013): 688-698.